

Dynamic modeling of reversible solid oxide cell stack and control strategy development

Botta, G.; Romeo, M.; Monteiro Fernandes, Álvaro; Trabucchi, S.; Aravind, P. V.

DOI

[10.1016/j.enconman.2019.01.082](https://doi.org/10.1016/j.enconman.2019.01.082)

Publication date

2019

Document Version

Accepted author manuscript

Published in

Energy Conversion and Management

Citation (APA)

Botta, G., Romeo, M., Monteiro Fernandes, Á., Trabucchi, S., & Aravind, P. V. (2019). Dynamic modeling of reversible solid oxide cell stack and control strategy development. *Energy Conversion and Management*, 185, 636-653. <https://doi.org/10.1016/j.enconman.2019.01.082>

Important note

To cite this publication, please use the final published version (if applicable). Please check the document version above.

Copyright

Other than for strictly personal use, it is not permitted to download, forward or distribute the text or part of it, without the consent of the author(s) and/or copyright holder(s), unless the work is under an open content license such as Creative Commons.

Takedown policy

Please contact us and provide details if you believe this document breaches copyrights. We will remove access to the work immediately and investigate your claim.

Dynamic modeling of reversible solid oxide cell stack and control strategy development.

G. Botta *, M. Romeo */**, A. Fernandes *, S. Trabucchi **/***, and P. V. Aravind*

*Delft University of Technology, Leeghwaterstraat 39, 2628 CB Delft, The Netherlands.

**Politecnico di Milano, Piazza Leonardo da Vinci 32, 20133 Milano, Italy.

***Delft University of Technology, Kluyverweg 1, 2629 HS Delft, The Netherlands.

Abstract - Solid oxide cell systems (SOCs) are increasingly being considered for electrical energy storage and as a means to boost the use of renewable energy and improve the grid flexibility by power-to-gas electrochemical conversion. The control of several variables (e.g., local temperature gradients and reactant utilization) is crucial when the stacks are used in dynamic operation with intermittent electrical power sources. In the present work, two 1D models of SOC stacks are established and used to investigate their dynamic behavior and to select and tune a suitable control strategy. Subsequently, safe operating ranges were determined to meet the thermal constraints of the stack by analysing not only the fuel cell (SOFC) and electrolyzer (SOEC) individual modes but also the switching between the two modes when the stack operates reversibly. The dynamic analysis shows that the control loops of our multi-input (reactant molar flow rates), multi-output (reactant utilization and maximum local temperature gradients) control system are strongly decoupled. Therefore, a proportional integral control strategy can be used to prevent dangerous stack operating conditions in dynamic operation. Finally, the controllers were tuned, and their transfer functions were reported. Convective heat transfer via air flow allows controlling the temperature of the solid structure of the cell/stack component, thus avoiding issues related to temperature variation during transient operation. Moreover, the reactant utilization controllers can avoid component fracture or degradation owing to fuel starvation under dynamic operation. The process can be approximated by two first order transfer functions. It can help in the design of more complex control systems in the future if necessary, with embedded process models, such as model predictive control. Results in the simulation environment are preparatory to the programming phase of an actual controller in real-world applications.

Index Terms – Dynamic Analysis, Renewable Energy, Reversible Solid Oxide Cells, Temperature and Reactant Utilization Control.

1 Introduction

Efficient electrical energy storage (EES) with power-to-gas solutions can play a substantial role in decarbonizing the electricity sector, integrating different energy grids and infrastructures, and increasing the penetration of renewable energy resources. Moreover, storing electricity in the form of chemical energy is advantageous owing to its long storage duration and flexibility [1].

Among EES technologies, solid oxide cell (SOC) systems are of considerable interest. These systems can store electricity by producing a synthetic fuel in the electrolysis (SOEC) mode and generate electricity by electrochemically oxidizing fuel in the fuel cell (SOFC) mode. Thus, they can balance the dynamic and decentralized nature of renewable sources and back up the grid. Furthermore, high-temperature SOECs are proven to be more efficient compared with a low-temperature electrolyzer [2].

Variable power demand can impose transients on the SOFC, which may be detrimental to long-term performance of the stack [3]. The performance of the fuel cell systems during transients is a key factor for its commercialization. In fact, two main bottlenecks should be addressed before introducing SOFC to commercial applications, that is, load following ability and durability [4]. The monitoring of stack transient response to load changes is fundamental to improve the durability, stability and performance of the device, thus safeguarding the stack operations. To generate a reliable and efficient power response and to prevent detrimental degradation of the stack voltage owing to reactant depletion and thermal stress, designing appropriate control strategies is crucial to maintain adequate inlet flow rates for fuel and heat management based on the current drawn from the SOFC stack. Understanding the fuel cells dynamic behavior and maintaining the operation of the entire system within desired constraints require control strategies implemented upon the fundamental understanding of the component dynamics. Huang et al. [4] presented a review of SOFCs, SOFC systems dynamic modeling, and model-based control. The review includes an overview of the control strategies and a general description of the control challenges in SOFCs. Szymd et al. [5] experimentally investigated the transient response of the cell voltage to a current ramp. They adopted a current-based fuel control to maintain a constant reactant utilization factor. The results show that the transient characteristics of the cell voltage are substantially affected by the local temperature gradients caused by manipulation of the current. Kupecki et al. [6] developed and validated via manufacturer's data a 1 kW-class SOFC stack. The model was used to predict the performance of the stack in co-, counter-, and cross-flow configuration. The same group investigated the potential to internally reform methane in an equal stack via a dynamic model and validated it experimentally [7, 8]. These studies showed that the effects of internal reforming on the outlet temperatures were detectable when the current is more than 22 A and that the temperature was maintained within the range recommended by the manufacturer. Ota et al. [9] evaluated an open-loop transient

60 response of a tubular SOFC to small load-step changes, whereas Achenbach et al. conducted a similar study for a
61 planar SOFC [10]. Aguiar et al. [11] presented a dynamic anode-supported intermediate-temperature direct
62 internal reforming one-dimensional SOFC model, which was also used by the same authors in a successive
63 work[3] to display the closed-loop response of the same fuel cell to step-load changes. The proposed PID
64 controller can maintain the desired outlet fuel temperature. Sedghisigarchi and Feliachi [12] developed a dynamic
65 model of a stand-alone SOFC plant to simulate the output voltage and temperature response to load step change,
66 to fuel step change, and to fast load variations. Pianko-Oprych et al. [13] developed a dynamic model of a power
67 generation system based on two SOFC stacks connected in series. The predictions of the model provide basic
68 insight into the behavior of the SOFC system during different transients. Chaisantikulwat et al. [14] presented a
69 SOFC dynamic model and a feedback control scheme. The output was retained under load disturbance by adjusting
70 the H₂ content in the fuel inlet. Mueller et al. [15] investigated the fuel cell voltage transient caused by the change
71 in H₂ concentration. The voltage transitory resulted to be in the order of seconds, whereas the temperature transient
72 is in the order of hours. Furthermore, the outcomes underlined the importance of controlling the fuel utilization
73 during transient operation. Cheddie and Munroe [16] constructed a one-dimensional model for real-time
74 simulation, indicating that the temperature difference across their cell outpaced 100 K.

75 Given that high reactant utilization is often required to enhance system efficiency and lower system operating
76 costs [17], improving the performance and durability of the SOFC stacks (but avoiding reactants depletion)
77 becomes essential. Lee S. et al. [17] developed and validated a three-dimensional physical model to examine the
78 effect of raising the fuel utilization on heat and mass transfer in SOFCs. The results show that when increasing the
79 fuel utilization, the electrochemical reaction zone is concentrated near the fuel inlet, leading to hydrogen depletion
80 in the downstream fuel flow, thereby inducing a large gradient of ionic current density along the cell. They also
81 depicted pressure gradients in the thickness and length direction of the cell owing to convective flow through the
82 porous electrodes, as well as a temperature gradient along the cell as a result of heat exchanges. The authors
83 claimed that these gradients can induce chemical, mechanical, and thermal stresses on the SOFC stacks, thus
84 inducing degradation. Bae Y. et al. [18] developed and experimentally validated a model for SOFC stacks to
85 evaluate the dynamic response of thermodynamic variables against electrical load changes. The results indicated
86 that the diffusion in the anode predominantly governs the overall transient behavior of the stack, whereas the
87 temperature requires a longer time to adjust itself to a new operating condition. Sorrentino M. and Pianese C. [19]
88 used a SOFC system model to design and test the control and energy management strategies. The proposed
89 approach is used in guaranteeing the targeted performance while keeping stack temperature derivative within safe
90 limits, and as a support to further development of control strategies. The same authors [20] reported the activities
91 performed within the European-funded project GENIUS, where general black-box models for modeling and
92 diagnosis of SOFC stacks were designed. The models were proven to be appropriate in performing real-time
93 monitoring and degradation analysis for various SOFC stack technologies. They are highly accurate and reliable
94 on both training and test datasets. Gallo et al. [21] developed a dynamic model called Diamond-A, which is used
95 for diagnosis and control of an integrated stack module based on SOFCs. The model simulates the behavior of a
96 non-conventional micro-CHP system, starting from operating variables. Marra et al. [22] developed a lumped
97 dynamic modeling approach for model-based control and diagnosis of a SOFC system with anode off-gas
98 recirculation. A 0-D lumped model approach was also used in [23] for a dynamic model of a methanol-driven fuel
99 cell system with an electric power of 350 W. The National Fuel Cell Research Center of the University of
100 California, Irvine (UCI), has extensively investigated the dynamic simulation and control system development for
101 SOFC cells and stacks, SOFC systems, and SOFC gas turbine hybrid systems. The authors studied various
102 parameters (i.e., operating conditions, inlet fuel gas, flow configurations, geometrical resolution, and time scales),
103 and they compared the developed models with the experimental data [24-35]. A summary of some of the works of
104 the same authors can be found in [36], where an approach for developing and applying dynamic simulation
105 techniques for SOFC and SOEC control system development can be retrieved.

106 Data-based modeling is used for the accurate dynamic estimation of SOFC stack temperature by Pohjoranta et
107 al. [37]. An empirical model is presented also by Leone and Lanzini [38]. In this study, they investigate the
108 transient operation of a large SOFC generator by using a system identification approach that is based on the
109 definition of a black-box model and on the identification of the main model coefficients based on actual
110 experimental data. Several languages and software are found in the literature for transient operation of fuel cell
111 stacks and systems. Dynamic SOFC system models based on the first physical principles, which describe system
112 phenomena via physical processes, and the use of multi-domain proprietary software such as MATLAB/Simulink
113 are presented in several works (e.g., in [39, 40]). Luo et al. [41] simulated a distributed system combining
114 renewable energy, natural gas, and energy storage on the basis of the commercial environment of gPROMS. The
115 non-proprietary modeling language Modelica is proven to be another appropriate option for SOFC system
116 modeling, as reported in [42, 43].

117 Intermittent electricity inputs, such as solar- or wind-generated electricity, result in a transient behavior of the
118 SOEC stack. For the SOFC, understanding the dynamic response of the stack is fundamental before the realization
119 of this technology. Luo et al. [44] studied the transient behavior of a tubular SOEC in the co-electrolysis mode
120 through modeling. The time constants of charge, and mass and heat transport processes were estimated. The
121 dynamic behavior was investigated by imposing the current, gas flow, and temperature step inputs. Through the
122 study, appropriate transient operations were designed to improve the efficiency and reactant conversions. Most of
123 the dynamic modeling studies on the response of a SOEC to transient inputs have been reported by the research
124 group of Brandon [45-47]. Udagawa, Aguiar and Brandon presented a one-dimensional cathode-supported SOEC
125 model [46]. The step changes in the average current density led to an alteration of the stack temperature in both
126 endothermic and exothermic operation. The same authors implemented a control strategy of the stack based on the
127 variation of air flow [48]. The changes in the average current density in the transient operation may indeed cause
128 a variation in the thermal regime of the stack, which may lead to unacceptable hot or cold spots. In [47], Cai et al.
129 demonstrated via modeling that the use of the air flow rate to control the temperature is successful, providing that
130 the change in current does not result in a transition from exothermic to endothermic operation of the SOEC. The
131 same group reported some preliminary results in [49] some for two control strategies during a change of the
132 operating regime to boost hydrogen production and eliminate electrical energy consumption.

133 State-of-the art research points out that the same SOC stack can be used in both fuel cell and electrolyzer mode
134 in a so-called reversible solid oxide cell (ReSOC) system. This electricity storage and production technology might
135 have high roundtrip efficiencies of 60%-70% and energy densities higher than that of the batteries [50, 51].
136 However, when operating reversibly, the thermal management is even more complicated than in the individual
137 mode because the thermal behavior of the stack is very different in fuel cell mode, when the reaction is always
138 exothermic, from that in the electrolysis mode, which corresponds to endothermic, exothermic or thermoneutral
139 reactions depending on the voltage. In addition, reversible operation causes the temperature distribution in the
140 stack to vary, leading to thermo-mechanical stresses. Electrodes and electrolytes of the SOC are characterized by
141 different thermo-mechanical properties and geometrical constraints, possibly leading to large thermal stresses
142 during thermal excursion and breakdown caused by rupture or buckling [52]. A new thermal management concept
143 of a ReSOC is presented by Di Giorgio and Desideri in [53], resulting in a roundtrip efficiency close to 70%. The
144 research group of Braun has conducted considerable modeling studies on the performance of ReSOCs [50, 54-58].
145 In their studies, ReSOCs are proposed for storing intermittent renewable energy and are studied in a steady-state
146 from different perspectives and various level of detail, after integrating their existing SOEC and SOFC models.
147 The same group presented the influence of the operating parameters considered crucial to transient response,
148 including inlet temperature, flow rate, and mass fractions in a single mode [54]. Klotz et al. [59] combined a
149 physical zero-dimensional model, which accurately describes the static behavior of the SOC under different
150 operating conditions, and a SOC performance model for large scales, to obtain precise predictions on the
151 performance and efficiency of SOC systems. Ferrero et al. [60] presented an integrated thermo-electrochemical
152 model for the simulation of polarization curves of ReSOCs, validating and calibrating it with an experimental test.
153 ReSOCs have also been investigated experimentally to comprehend the aging and degradation of the materials and
154 to verify concepts and simulations. At the Julich research center, a two-cell planar stack was developed and
155 operated for 4000 h in fuel cell, for 3450 h in steam electrolysis, and for 640 h in co-electrolysis modes [61] to
156 illustrate the preliminary results on long-term aging. Sar et al. also presented a durability test on a coral
157 $\text{Ce}_{0.9}\text{Gd}_{0.1}\text{O}_{2-\delta}\text{-La}_{0.6}\text{Sr}_{0.4}\text{Co}_{0.2}\text{Fe}_{0.8}\text{O}_{3-\delta}$ -doped electrode-supported cell for a shorter time (i.e., 430 h as
158 SOEC and 350 h as SOFC) [62]. Sanz-Bermejo et al. reproduced and enhanced a SOEC system in partial load
159 conditions, thus evaluating its performance with constant steam utilization, constant inlet steam flow rate, constant
160 inlet gas temperature, and constant thermoneutral electrolysis operation [63]. Petipas et al. investigated the
161 behavior of a SOEC system, combined with a 1.35 MW solar farm, under transient operating condition [64]. Their
162 results revealed that the average system efficiency over one year was 92%. The same authors conducted several
163 tests to explore the steady-state and dynamic performance of a single SOEC [65]. Moreover, the same group
164 evaluated the steady-state behavior of a SOFC system without external heat source under various loads [66].
165 Sunfire GmbH performed a stack test with 26 cycles switching between SOFC and SOEC mode at low current
166 density (0.3-0.4 A/cm²). The stack presented a 0.06% degradation per ReSOC cycle [67]. Graves et al.
167 demonstrated that critical electrolysis-induced degradation can be erased by the cycling between electrolysis and
168 fuel cell modes [68].

169 Certainly, the operation of ReSOCs might be subject to frequent load changes. Transient events, such as start-
170 up and shutdown, are certain for both the stacks intended to operate at steady state and that under load-following
171 operation. However, dynamic studies on ReSOCs are hardly available in the current literature, and the ReSOC
172 transient response is not yet well understood. In fact, when considering the ReSOC, most of the efforts so far have
173 focused on improving the properties of its materials (e.g., power density, catalysts activity, electrolyte conductivity,
174 etc.), or describing its steady-state performance. Meanwhile, the understanding of the ReSOC dynamics toward
175 the objective of control application has not been a main consideration until recently. Nonetheless, dynamic analysis
176 is essential for the stack design and definition of appropriate control strategies. Zengh et al. [69] presented a one-

177 dimensional model to investigate the basic dynamic processes of ReSOCs, particularly that involved in switching
178 mode, to finally provide a basic guide to control the ReSOC stack. A 2D transient model of ReSOC was developed
179 by Jin X. and Xue X. to investigate the overshoot parameters during the switching mode [70]. Ma R. et al. designed
180 a ReSOC model, validated experimentally under different operating conditions, for real-time simulation or online
181 diagnostic control [71]. Er-rbib et al. [72] developed a dynamic model to study the ReSOC in transient behavior.
182 The results show that the thermal inertia of the cell causes a temperature peak in the dynamic operation.

183 ReSOC systems can be a cost-effective, highly efficient EES, but many questions still need to be answered
184 [53]. One of the most challenging problems is stack durability owing to thermal stress or decreased content of
185 reactants. Experimental results demonstrated a correlation between stack temperature and ambient temperature
186 perturbations [36], leading to the need of an appropriate dynamic control. To extend the lifetime of the SOC stack,
187 its local temperature gradients must be maintained within a certain range [3, 13, 73]. Therefore, the temperature
188 control strategy becomes important to prevent a deleterious stack mechanical stress and catalyst migration owing
189 to thermal excursion. In addition, the temperature control strategy can assist in maintaining a constant operating
190 condition (i.e., endothermic, exothermic, or thermoneutral) of the stack and consequently simplifying the system
191 design. An adequate reactant utilization control strategy is important to avoid dramatic increases in the utilization
192 rate, thus irreversibly damaging the stack. Moreover, to implement the frequent switch between generation and
193 storage, a deep understanding of the dynamic is necessary in both individual modes and transitional processes.
194 Only few studies have been conducted to investigate the complex dynamic processes of the ReSOC, and further
195 studies on mode switching are essential to obtain a more comprehensive understanding.

196 This study aims to present the dynamic behavior of a ReSOC and to discuss its control strategies. The work
197 introduces a dynamic analysis of the ReSOC stacks, investigating not only the SOFC and SOEC individual mode,
198 but also the switching between the two modes when the stack operates reversibly. Investigating the transient
199 responses aids in defining the key parameters influencing the dynamic behavior of the stack. Temperature and
200 reactant utilization control are crucial when the stacks or systems are used in dynamic operation with intermittent
201 electrical power sources. Fuel starvation and temperature variation during transient operation might lead to
202 component fracture or degradation. Therefore, a model is used to define the control parameters for transient
203 operations to avoid these issues. The study investigates the potential of controlling the temperature variation and
204 reactant utilization of the stack through the change in the air and fuel flow rates. Finally, the controllers are tuned
205 and their transfer functions reported to better understand the physical behavior of the stack.

206 To the best of our knowledge, this work presents a significantly detailed analysis of a ReSOC stack from the
207 control perspective, in comparison with the existing literature on ReSOCs, and it details the influence of control
208 strategies on the ReSOC safe operation. In fact, the stack is first analyzed regarding the linearized system and
209 transfer functions, and later control algorithms in closed-loop fashion are tuned and tested in the simulation
210 environment. This work also distinguishes itself from previous research and development efforts in the use of
211 closed-loop controllers, as opposed to open-loop controllers commonly adopted to verify the accuracy of the
212 control action. Closed-loop control is expected to provide automated correction steps to process disturbances. thus
213 helping in maintaining the stack safety and meeting the demands from the power system to which it is connected.
214 As and when the ReSOCs are connected to future grids drawing power from intermittent renewable energy sources,
215 a proper system control is expected to be immensely important. Hence, the authors believe that the efforts presented
216 in this manuscript are well justified.

217 **2 Methodology**

218 One-dimensional distributed dynamic models of electrode-supported SOC stacks were developed and their
219 reliability was evaluated. Subsequently, safe operating ranges for the SOFC and SOEC were defined, including
220 the definition of nominal, minimum, and maximum current densities for each mode. The minimum current
221 densities of the individual modes were selected as boundary conditions when studying the ReSOC response to
222 transient conditions. Furthermore, a dynamic analysis was conducted for all the operating modes described above.
223 As previously mentioned controlling the temperature and the reactant utilization to prevent cell/stack degradation
224 in transient states is crucial. Therefore, a control strategy was designed on the basis of the transients analysis to
225 ensure the function of the stack within safe operating condition and to maintain a secure utilization rate. The
226 controller transfer function was finally studied and tuned to guarantee the stability of the stack. Figure 1 illustrates
227 how the work was implemented.

228 **Figure 1 Representation of the manuscript work flow diagram**

230 **2.1 Model development**

231 Based on a SOFC template available in *Modelon* library, the SOEC was modeled using *Modelica* [74], an open-
232 source, equation-based language for the modeling of systems described by differential-algebraic equations
233 (DAEs). It was simulated via the commercial software *Dymola*. Owing to the object-oriented nature of the

234 modeling language, different phenomena (e.g., electrical, thermal, and chemical) were simulated at the same time
235 and sub models with different complexity levels were easily manipulated. Both the SOFC and SOEC models
236 contain reactions, electrochemistry and mass balance for the gas streams. A temperature state is introduced, and
237 the energy balance is defined. The models allow in studying the effect of cell geometry, operating conditions, and
238 inlet gas composition.

239 The cells are electrically and thermally connected in series to model a substack, whereas the complete stack is
240 constructed assembling in parallel several substacks. According to the symmetry of SOFCs and SOECs, the two
241 individual models have been integrated by the authors, considering the logic of *Modelica*, to create a ReSOC model
242 and evaluate the transients during switching modes. The operating mode (SOFC or SOEC) is defined by varying
243 the sign of the current densities. When the current density is negative, the stack operates in electrolyzer mode. The
244 models use the finite volume method, where every component is discretized in space via control volumes [75],
245 thus allowing the model to achieve any desired spatial resolution. This geometric simplification has been presented
246 and compared with experimental data in many previous works [25, 26, 31]. The modeling scope can be decreased
247 considering symmetry within the stack and within the repeating units of the stack [36].

248 The main performance characteristics (e.g., temperature and current density) cannot be well estimated
249 without determining the spatial variations in species concentrations, temperature, etc. The model should capture
250 the chemistry, electrochemistry, and physical spatial dependence without overloading the computational effort.
251 Therefore, determining the limited spatial resolution becomes crucial to resolve the geometry for capturing the
252 directions in which these parameters vary considerably [36].

253 2.1.1 Primary model assumptions

254 The main assumptions and key simplifications are as follows:

- 255 ▪ Co-flow configuration, which assumes a uniform distribution of gas flow.
- 256 ▪ Only one spatial dimension (axial direction) is considered [36].
- 257 ▪ Ideal gas law is assumed.
- 258 ▪ The cell-to-cell variations are typically very small [36]. Each cell in the stack is assumed to operate with equal
259 flows and current. Therefore, the heat transfer between cells in the stack is neglected.
- 260 ▪ Pressure drop along the gas channels is neglected.
- 261 ▪ Temperature gradient is considered only along the flow direction; the heat is transferred only between the cell
262 solid parts and the gas streams (air and fuel channels). Newton's law is used to determine the convection heat
263 transfer between the solid and gas control volumes, expressed in Equation (9).
- 264 ▪ Fluid properties vary along the channel, and they are evaluated in each discretization volume of the channel.
- 265 ▪ Each control volume accounts for local conditions and it is characterized by a lumped temperature, pressure,
266 and species mole fractions; these are assumed to be the mean values of the same control volume.
- 267 ▪ Current density is appraised in each discretization volume along the cell, because heat generation is not uniform
268 along the flow direction, but it varies in each discretization volume [3, 46, 76].
- 269 ▪ Current changes are assumed to occur instantaneously during the simulations [16].
- 270 ▪ The stack is assumed to be insulated from the environment.
- 271 ▪ The unit cell is considered to consist of three components, namely, fuel and air streams, and solid structure
272 (including two electrodes, air and fuel electrodes, and electrolyte). The cathode electrolyte anode assembly is
273 referred as positive electrode electrolyte negative electrode (PEN). The interconnects are considered part of the
274 two channels, as shown Figure 2.
- 275 ▪ Nernst potential is calculated at the inlet condition in each discretization volume.

276

277

278

Figure 2 Graphical representation of the planar unit cell [11]

279 2.1.2 Main SOC model governing equations

280 Most of the equations and properties are defined at the cell level. A simplified electrochemical model is used
281 to relate the gas species concentrations, cell temperatures, and current density to the cell voltage. Then, the cell
282 voltage can be used to calculate the electrical energy consumed or produced. The cell voltage (V_{cell}) corresponds
283 to the sum of the reversible potential and the irreversible losses that occur when the current crosses the cell. The
284 area specific resistance (ASR) accounts for the irreversible losses. The reversible potential is defined as the Nernst
285 potential (V_{Nernst}), which is the minimum electrical potential required to split H_2O when the cell operates at a
286 specific temperature and with a distinct gas concentration. The thermoneutral voltage (V_m) represents the operating
287 point of the SOEC, where the heat consumed by the reactions is exactly balanced by the heat generated via
288 irreversible losses.

289 The compositions of the fuel and air streams evolve along the cell. In the energy balance, the heat exchanges
290 among the gas streams and the solid parts of the cell are considered fully convective.

291 Reactant utilization (U) and inlet air to fuel mole ratio (γ) are defined at the substack level.

292 The maximum local temperature gradients along the cell (∇T_{max}), which is crucial to determine the safe
 293 operating range of the stack, is defined by the authors at the stack level and described in Equations (14) and (15).

294 The dynamic equations are solved in each control volume. The main equations involved in the models are
 295 presented in Table 1-Table 5, whereas the remaining equations can be found in [75]. Interactive procedures are
 296 applied through a differential-algebraic system solver method to solve the system of algebraic and differential
 297 equations.

298 **Table 1 Reactions defined at cell level**

Reaction	Chemical equations
Fuel electrode	$H_2O+2e^- \rightarrow H_2+O^{2-}$ (1)
	$H_2+O^{2-} \rightarrow H_2O+2e^-$ (2)
Air electrode	$O^{2-} \rightarrow 1/2O_2+2e^-$ (3)
	$1/2O_2+2e^- \rightarrow O^{2-}$ (4)

299 **Table 2 Equations for electrochemistry, and heat transfer defined at cell level**

Variables	Equations
V_{Nernst}	$V_{Nernst}(x) = \frac{\Delta_{\bar{g}}}{2F} + \frac{RT_{cell}(x)}{2F} \ln\left(\frac{p_{H_2}(x)p_{O_2}^{0.5}(x)}{p_{H_2O}(x)p_{ref}^{0.5}(x)}\right)$ (5)
ASR	$ASR(x) = ASR_0 \exp\left[\frac{E_a}{R}\left(\frac{1}{T_{cell}(x)} - \frac{1}{T_0}\right)\right]$ (6)
V_{cell}	$V_{cell} = V_{Nernst} \pm I_{cell} \frac{ASR}{A_{cell}}(N)$ (7)
V_{tn}	$V_{tn} = \frac{\Delta_{\bar{h}}}{2F}$ (8)
\dot{Q}_{conv}	$\dot{Q}_{conv}(x) = \frac{A_{cell}}{N} h_{conv} dT(x)$ (9)

301 Note: $\Delta_{\bar{h}}$ = molar enthalpy of the reactions, $\Delta_{\bar{g}}$ = difference of molar Gibbs free energy for the reactions, F = Faraday's constant, R =
 302 universal gas constant, T_{cell} = cell operating temperature, N = number of discretization volumes, P_{ref} = cell operating pressure, p_i = partial
 303 pressure of each species, A_{cell} = cell surface, ASR_0 = initial temperature-dependent value, constant area specific resistance at temperature T_0 ,
 304 T_0 = reference temperature of ASR_0 , E_a = activation energy, h_{conv} = convective heat transfer coefficient.

305 **Table 3 Temperature state and energy balance defined at cell level**

Variables	Equations
$\frac{dT_{cell}}{dt}$	$\frac{dT_{cell}}{dt}(x) = \frac{\dot{Q}_{airele}(x) + \dot{Q}_{fuelele}(x) + \dot{Q}_{wall}(x) + \dot{Q}_{cell}(x)}{mc_p}(N)$ (10)
\dot{Q}_{cell}	$\dot{Q}_{cell}(x) = \dot{H}_{airele}(x) + \dot{H}_{fuelele}(x) + P_{cell}(x)$ (11)

307 Note: \dot{Q}_i = heat exchanged through each thermal interface of the cell, m = cell mass, c_p = specific heat capacity at constant pressure, \dot{H}_i =
 308 enthalpy flow. $\dot{Q}_{wall} = 0$ since interconnects (wall) and solid structure (PEN) are assumed at the same temperature.

309 **Table 4 Reactant utilization and air ratio defined in SOEC at substack level**

Variables	Equations
U	$U = \frac{\dot{n}_{H_2O}^{in} - \dot{n}_{H_2O}^{out}}{\dot{n}_{H_2O}^{in}} = 1 - \frac{\dot{n}_{H_2O}^{out}}{\dot{n}_{H_2O}^{in}}$ (12)
γ	$\gamma = \frac{\dot{n}_{air}^{in}}{\dot{n}_{fuel}^{in}}$ (13)

311 Note: \dot{n}_i = molar flow of each species.

312 **Table 5 Maximum temperature gradient along the stack defined at stack level**

Variables	Equations
∇T_{max}	$\nabla T_{max} = \max(\nabla T_{stack})$ (14)
∇T_{stack}	$\nabla T_{stack} = \begin{pmatrix} \nabla T_{1,1} & \nabla T_{1,2} & \dots & \nabla T_{1,N-1} \\ \nabla T_{2,1} & \nabla T_{2,2} & \dots & \nabla T_{2,N-1} \\ \vdots & \vdots & \ddots & \vdots \\ \nabla T_{M,1} & \nabla T_{M,1} & \dots & \nabla T_{M,N-1} \end{pmatrix}$ with $\nabla T_{i,j} = \nabla T_{i,j} - \nabla T_{i,j-1}$ (15)

315 Note: M = number of substacks.

316 318

317 To ensure cell integrity, evaluating the temperature and heat transfer and monitoring the temperature gradients
 318 of each control volume along the cell, and not only of the entire cell, are necessary. The temperature gradient is
 319 determined in resolving Equation (10), which refers to the conservation of energy. From the state space
 320 representation of temperature and species mole fractions, the thermodynamic properties are evaluated, and the
 321
 322

323 models can predict the dynamic performance, heat transfer extent, flows, and work generated or consumed locally
324 through the cell/stack.

325 **2.2 Model verification**

326 Although the basic *Modelon* model was validated in [77], both SOFC and SOEC models are first compared
327 with the results obtained from Cheddie et al. [16] and Udagawa et al. [46] to evaluate their accuracy. In this case,
328 as done previously in [46], the model of the unit cell is supposed to be located at the center of a large stack; thus,
329 no edge effects are observed. Heat was exchanged only between the cell and gases in the air or fuel channels. This
330 assumption is frequent in the literature because with the proper use of boundary conditions, the behavior of a
331 single cell is assumed to describe the response of an entire stack [48]. In the simulations run to check the reliability
332 of our model, the reference ASR_0 values were taken consistently with the literature [16, 46].

333 Similar trends were obtained, and the maximum relative error when predicting the operating voltage before
334 and after an instantaneous current change was in the range of 3%-5%. The maximum relative error on the transient
335 temperature along the flow direction was between 1% and 2% for different average currents. The slight differences
336 in the results were associated with the diverse approaches used to simulate the irreversibility of the cell and the
337 heat transfer mechanisms. Regarding the latter, constant heat transfer coefficients were specified in our work,
338 whereas in [46] these coefficients are calculated from a constant Nusselt number for the flow temperature.
339 Nevertheless, for the operational range of temperatures, the values for these coefficients are of the same order of
340 magnitude. Moreover, in our model the Nernst voltage is computed using the bulk composition of the gas in the
341 flow channel rather than at the triple phase boundary.

342 The precision of the ReSOC model response to transients was verified by comparing its results with the
343 behavior of the stack in both operational modes, which were simulated via the two individual models, that is SOFC
344 and SOEC.

345 For the details of the comparisons used to verify the reliability of the models refer to Figure 3 and Figure 4.

346

347 **Figure 3 Comparison between the values obtained from our SOEC cell model and that predicted in [46] when evaluating the cell
348 voltage for different average current densities and cell temperature along its length**

349

350 **Figure 4 Comparison between the values obtained from our SOFC cell model and that predicted in [16] when evaluating the cell
351 voltage and cell temperature in the last volume of control, before and after an instantaneous change in current**

352 **2.3 Safe operating range definition of SOC stack, operating conditions, and main physical 353 assumptions**

354 After the reliability of the model was verified, the safe operating range of the stack was defined. Initially, the
355 physical and geometrical stack characteristics are defined and fixed. When defining the safe operating range, the
356 stacks were fed with a constant flow of H_2O/H_2 mixture. The maximum utilization factor was set to 75% to avoid
357 structural damages to the stack [47]. The air flow entering the stack was also constant, but three different cases
358 were analyzed, with γ equal to 8, 12, 16 and 0.8, 1.6, 2.4 evaluated for the SOFC and SOEC, respectively. These
359 values were chosen in accordance with the previous studies [11, 45, 46, 48, 50].

360 The stack operates at ambient pressure and the inlet mixtures are set to 750 °C in the channels of both
361 electrodes. The stacks undergo a current density ramp, sufficiently slow to go through all the steady-state points,
362 of 1000-10000 and 1000-15000 A/m² for the SOFC and SOEC, respectively. The initial values were chosen in
363 accordance with the previous studies [54, 78-80]. Similar to what was reported in [3] and [73], all the current
364 density values for which the maximum local temperature gradient (∇T_{max}) was lower than 10 K/cm were selected
365 as the safe operating range. This maximum local temperature gradient results from a thermal expansion coefficient
366 of 10⁻⁵/K and a maximum safe stress-induced strain of 0.1%, as reported in [52]. In fact, the probability of cell
367 failure increases drastically for localized solid structure temperature gradients more than 10 K/cm [81].

368 For each value of γ , a maximum allowable current was determined. Higher values of γ lead to higher maximum
369 current densities, owing to larger heat transfer capability. The nominal current was set to ~75% of the maximum
370 current for the SOEC and ~60% for the SOFC. The minimum current of both corresponds to ~50% of the maximum
371 current, in accordance with [50, 82, 83].

372 The number of discretization volumes (N) was chosen on the basis of the trade-off between computational time
373 and accuracy of the results, in accordance with the literature [36]. Andersson et al. demonstrated that by increasing
374 the number of control volumes from 4 to 50, the error reduces in only 1.4% [77]. In all the simulations, the
375 reference ASR_0 value was taken in accordance with that in the literature [78, 82, 84, 85].

376 The main physical parameters and specifications assumed to define the safe operating range when the stack
377 operates in SOEC or SOFC are presented in Table 6.

378

379

Table 6 Stack operating condition and parameters to determine the safe working range [46, 82, 86, 87]

Stack parameters	
Stack mass [kg]	220
# of cells per substack [-]	50

# of substacks in the stack [-]	2
# of discretization volumes [-]	10
Cell parameters	
Cell area [m ²]	0.04
Cell length [m]	0.4
Cell thickness [μm]	500
Cell density, ρ_{cell} [kg/m ³]	5900
Total cell mass, m_{cell} [kg]	0.3
Specific heat capacity, c_p [kJ/kgK]	0.5
Reference ASR ₀ [Ωcm ²]	0.35 x 10 ⁻⁴
Reference temperature, T ₀ [°C]	750
Activation energy, E _a [J/mol]	62715.5
Convective efficient solid-gas control volume h_{conv} [W/m ² K]	250
Fuel and air channel geometric parameters	
Fuel channel height [mm]	1
Air channel height [mm]	1
Interconnect thickness [μm]	500
Interconnect density, ρ_{int} [kg/m ³]	8000
Gas mixture condition at the SOFC and SOEC stacks inlet	
Pressure [bar]	1
H ₂ -H ₂ O inlet temperature [°C]	750
Air inlet temperature [°C]	750
Steam molar fraction [-]	0.45
Hydrogen molar fraction [-]	0.50
Inert gases in fuel electrode [-]	0.05
Stack operating conditions	
Current density evaluated SOEC [A/m ²]	1000-15000
Current density evaluated SOFC [A/m ²]	1000-10000
Max. H ₂ /H ₂ O utilisation	75%
Stoichiometry	
Values of γ analyzed in SOEC	0.8-1.6-2.4
Values of γ analyzed in SOFC	8-12-16

380 Note: The software requires a minimum concentration of all the compounds present in the fuel cell package library to avoid numerical
381 errors. However, inert gases do not participate in any reaction of the SOCs.

382 2.4 Dynamic analysis, and control strategy selection and evaluation

383 The authors developed a SOC dynamic model and a control strategy to maintain safe local temperature
384 gradients and a constant reactant utilization despite load changes. Dynamic responses are determined as the result
385 of coupled DAEs derived from conservation laws. The control system is a multi-input, multi-output (MIMO)
386 system. Then, a set of equations are numerically linearized to obtain the system transfer functions between the
387 manipulated ($\dot{m}_{fuel}, \dot{m}_{air}$) and controlled ($U, \nabla T_{max}$) variables in which the control loops are closed. This is the
388 first step of the control system design according to the classic control theory [88, 89]. The matrix of the Laplace
389 transfer functions is reported, as expressed in Equation (16). Via *MATLAB* the authors obtained successively the
390 Bode diagrams of the matrix of the transfer functions $G(s)$.

391 The control strategy to ensure the running of the stack within the operating safe range and at 75% utilization
392 rate is designed based on the analysis of transients, so that both the stability and control goals are achieved. In the
393 case of a MIMO system, a simple control strategy can be implemented if the control loops are decoupled. If this
394 condition is met, then a PID controller can be employed to control the stack; such controller has a proportional
395 (P), integral (I), and derivative (D) action.

396 In the P-only control, the controller output is usually determined from the product of the controller gain (K_p),
397 and the offset. Generally, the P-only control is characterized by the steady-state errors that occur after a change in
398 the set-point during the transients, or disturbance. This offset can be eliminated by incorporating the integral action,
399 (T_i) within the proportional controller.

400 The most suitable analytical tool to quantify the mutual influence of the two possible control loops is the
401 relative gain array (RGA) matrix. The interested reader can refer to [88] for the theoretical analysis of the problem
402 in the classic theory framework. The RGA of our MIMO system resulted strongly decoupled in both the SOFC
403 and SOEC (Table 9). As a consequence, two separated control loops were adopted. A proportional integral (PI)
404 control strategy is chosen, as phase anticipation via derivative action in our case is not required. The PI transfer
405 function is defined by R(s), connected in a classic closed-loop fashion, as shown in Figure 5.

406
407 **Figure 5 Study control volume: two control loops with PI controller. (SP=Set point)**
408

409 The main equations of the dynamic analysis and control strategy definition are reported in Table 7. Equation
410 (17) represents the loop transfer functions $L(s)$. To obtain the parameters for control tuning, the system of equations
411 (18) is solved in K_p and T_i for both control loops [88, 90].

Because of stability issues (Bode criterion), the maximum crossover frequencies ω_c obtained, which represent the promptness of the control loop, are 0.1 rad/s for utilization rate and 0.01 rad/s for temperature gradient. A phase margin of 80° is set to avoid oscillations in the controlled variables.

The minimum currents obtained when selecting the safe operating range for the SOEC and SOFC, with $\gamma=1.6$ and $\gamma=12$, respectively, are employed as boundaries for the ReSOC operating currents range, evaluated during its dynamic analysis. The ReSOC stack undergoes a current ramp of 0.5 A/min, which is set as nominal value. When studying the behavior of the ReSOC stack under transient operation, the main operating condition and the physical assumptions are the same listed in Table 6. However, in this case, the simulations are not run considering a stack of multiple cells, but rather a large stack containing a single cell in its center, which is assumed to represent the response of the whole stack in line with the studies presented by Brandon's group [76]. The same model was used to analyze the steady-state behavior of the cell, in endothermic and exothermic operation, evaluating for different average current densities the electrochemical and thermal variables of the cell along its length.

Table 7 dynamic and control analysis equations

Dynamic and control model	Equations
Matrix of transfer functions	$G(s) = \begin{bmatrix} \frac{\Delta U(s)}{\delta \dot{m}_{fuel}(s)} & \frac{\Delta U(s)}{\delta \dot{m}_{air}(s)} \\ \frac{\Delta(\nabla T_{max})(s)}{\delta \dot{m}_{fuel}(s)} & \frac{\Delta(\nabla T_{max})(s)}{\delta \dot{m}_{air}(s)} \end{bmatrix} = \begin{bmatrix} G_{11}(s) & G_{12}(s) \\ G_{21}(s) & G_{22}(s) \end{bmatrix} \quad (16)$
Control loop transfer function	$L(s) = R(s)G(s) \quad (17)$
System for control tuning	$\begin{cases} L(j\omega_c) = 1 \\ \varphi_m = 180^\circ - \varphi_c = 80^\circ \end{cases} \quad (18)$

3 Results and discussion

3.1 Dynamic analysis and control tuning results, for a SOFC and a SOEC stack of 100 cells

The maximum safe operating current and its relative nominal and minimum value are reported for the SOEC and SOFC in Table 8.

Table 8 maximum, nominal and minimum current density for SOCs

SOEC	$\gamma=0.8$	$\gamma=1.6$	$\gamma=2.4$
Maximum Current Density [A/m ²]	13465	13963	14685
Nominal Current Density [A/m ²]	10098	10500	11013
Minimum Current Density [A/m ²]	6732	6700	7342
SOFC	$\gamma=8$	$\gamma=12$	$\gamma=16$
Maximum Current Density [A/m ²]	5863	6735	7310
Nominal Current Density [A/m ²]	3518	4050	4386
Minimum Current Density [A/m ²]	2932	3250	3655

RGA matrices for the SOFC and SOEC, evaluated at the nominal operating points, and the relative matrices containing the gains of all the transfer functions ($\mu(G)$) are reported in Table 9. The order of magnitude presented in the table indicates the influence that the manipulated variable (at the denominator) has on the controlled variable (at the numerator). For instance, the air molar flow has a minimal impact on the fuel utilization; therefore, the resulting value has an order of magnitude lower than 10^{-5} . The values obtained in the matrix are not equal to zero because the air flow rate indirectly affects the fuel utilization by affecting the temperature.

Table 9 RGA matrices and gains of the transfer functions for SOFC and SOEC

SOEC	RGA matrix	$\mu(G)$
	$\begin{bmatrix} 9.99 * 10^{-1} & 1.31 * 10^{-8} \\ 1.31 * 10^{-8} & 9.99 * 10^{-1} \end{bmatrix}$	$\begin{bmatrix} -3.16 * 10^2 & 1.21 * 10^{-7} \\ -2.01 * 10^3 & -6.77 * 10^1 \end{bmatrix}$
SOFC	RGA matrix	$\mu(G)$
	$\begin{bmatrix} 9.99 * 10^{-1} & 6.82 * 10^{-8} \\ 6.82 * 10^{-8} & 9.99 * 10^{-1} \end{bmatrix}$	$\begin{bmatrix} -1.27 * 10^2 & 2.34 * 10^{-5} \\ -1.18 * 10^3 & -3.18 * 10^3 \end{bmatrix}$

The dynamic analysis shows that in SOEC operation the increase in air mass flow rate strongly influences the ∇T_{max} , while in SOFC operation, this aspect is less pronounced owing to the strong exothermic behavior close to cell inlet. Nonetheless, an increase in air flow will result in a mitigation of the thermal gradients along the flow direction. In fact, the air flow rate affects the flow velocity in the air side, and therefore, the heat advection. As a consequence, the air flow rate varies and the temperature of the solid part decreases or increases by convection. The Bode diagrams for the transfer functions of the SOFC and SOEC are shown in

Figure 6.

Figure 6 Bode diagrams of the transfer functions of the SOEC and SOFC stacks

By having a closer look at the Bode diagrams reported in Figure 6, it is easy to notice that the two process transfer functions, $G_{11}(s)$ and $G_{22}(s)$, can be both approximated by a first order transfer function in the frequency range of interest. Particularly, the first one can be represented by a zero-pole function, Equation (19)), where the zero has a positive real part. In fact, while the gain is almost constant up to 100 rad/s owing to the opposite effect of zero and pole, the phase loses 180° . The second one can be represented by a simple first-order transfer function with a single pole (Equation (20)). In this case, the gain decreases at a rate of -20 dB/decade steadily up to 1 rad/s, while the phase loses 90° . The extrapolation of the transfer function time constants and gains is out of the scope of this study, but it is interesting that such a complex process can be approximated by two first order transfer functions. This aspect could enable in the future the design of more complex control systems if necessary, with embedded process models, such as the model predictive control (MPC).

The RGA matrix of our MIMO system was strongly decoupled both in the SOFC and SOEC. As a consequence, two separated control loops were adopted. The $G(s)$ step response analysis is presented in Appendix A. The parameters for control tuning (i.e., the proportional gain K_p and the integral time T_i) are obtained and listed in Table 10.

Table 10 Controllers parameters for SOFC and SOEC

SOEC	K_p [-]	T_i [s]
U	$-7.858 \cdot 10^{-7}$	0.001
∇T_{max}	$-1.63 \cdot 10^{-3}$	335.8
SOFC	K_p [-]	T_i [s]
U	$-3.163 \cdot 10^{-7}$	0.001
∇T_{max}	$-4.28 \cdot 10^{-2}$	232.4

Table 11 Simplified process transfer functions

Variables	Equations
Simplified $G_{11}(s)$	$G_{11}(s) \sim \mu_{G11} \frac{1 - \tau s}{1 + T_1 s}$ (19)
Simplified $G_{22}(s)$	$G_{22}(s) \sim \mu_{G22} \frac{1}{1 + T_2 s}$ (20)

The settling time of the closed-loop transfer functions ($L(s)$) is defined as $5/\omega_c$ [88]. Thus, for both SOFC and SOEC stacks, considering the ω_c obtained (i.e., 0.1 rad/s for utilization rate and 0.01 rad/s for temperature gradient), it takes to the controller around 50 s to stabilize the reactant utilization, while it brings the ∇T_{max} back to its set-point over a longer time, approximately 500 s.

3.2 Simulation results and discussion for ReSOC stack

The behavior of a single cell is assumed to describe the response of an entire stack [48]. In all the dynamic simulations (sections 3.2.1-3.2.3), the cell was allowed to reach the steady-state operation at 6700 A/m^2 before the ramp was applied to evaluate the cell behavior exclusively during the transition between the two operation modes, from 6700 A/m^2 (SOEC operation) to 3250 A/m^2 (SOFC operation). Only the time necessary to reach the new steady state after reaching the end of the ramp was determined. The cell was operated with an inlet air and fuel streams temperature of 750°C . When the local temperature gradients on the solid structure of the cell are within the safe limit, the controller, when present, does not manipulate the air flow. The constant minimum air flow in the SOFC is 10^{-4} kg/s and in the SOEC is 10^{-5} kg/s . Between -1500 A/m^2 and 1500 A/m^2 , the controller, when present, does not manipulate the reactant flow, and a minimum constant reactant flow of 10^{-5} kg/s is provided to avoid operating the cell without any gas. Table 12 lists the tuned controller's gain and integral time for the ReSOC when a ramp of 0.5 A/min in the average current density from 6700 A/m^2 (SOEC operation) to 3250 A/m^2 (SOFC operation) is imposed.

Table 12 Control tuning parameters for ReSOC

SOEC	K_p [-]	T_i [s]
U	$-6 \cdot 10^{-6}$	20
∇T_{max}	$-1 \cdot 10^{-4}$	50
SOFC	K_p [-]	T_i [s]
U	$-5 \cdot 10^{-6}$	20
∇T_{max}	$-6 \cdot 10^{-4}$	850

Small K_p values, such as those obtained, imply a high gain of the transfer functions. In other words, a small variation in the air and fuel flow rates entails a significant variation of reactant utilization and local temperature

493 gradients. This highlights once again the crucial importance of a control strategy to prevent issues of cell
494 degradation. Local temperature and reactant utilization control is required to maintain the cell within safety
495 boundaries during transient changes in the current density.

496 In addition, a steady-state analysis (section 3.2.4) was conducted to evaluate the behavior of the ReSOC local
497 temperature gradient, temperature profile, cell voltages, ASR, and local current density along the cell length. The
498 cell with the developed controller was operated with an inlet air and fuel stream temperature of 750 °C and at
499 average current densities of 3250 A/m² (SOFC), 6700 A/m² (slightly exothermic SOEC), and 5000 A/m²
500 (endothermic SOEC).

501 3.2.1 Dynamic behavior of ReSOC under transient operation, with and without controllers

502 A series of dynamic simulations is run to predict the cell behavior with or without the implementation of the
503 local temperature gradient control. The cell is fed with a constant and small air flow, a constant and large air flow
504 and a controller manipulated air flow, (Figure 7a). The ∇T_{\max} for the chosen ramp (0.5 A/min) is evaluated for all
505 cases (Figure 7b). The dynamic results for the simulation with a constant small air flow (no control) show
506 dangerous solid-structure local temperature gradients, which are associated with the increase in current density in
507 the SOFC mode. A sudden rise in ∇T_{\max} is depicted at most of the evaluated current densities when working in the
508 SOFC, and local temperature gradients above the maximum local ∇T_{\max} allowed (10 °C/cm) are observed. At a
509 current density of 3250 A/m², ∇T_{\max} reaches 30 °C/cm. When working with a constant air flow rate, which is set
510 equal to the maximum value obtained via the controller to face the current at 3250 A/m², the temperature becomes
511 stable within the safe bounds for the entire current range. Evidently, the excess of air protects the cell. In this
512 scenario, the local ∇T_{\max} is below 7 °C/cm for the whole ramp. However, in a real system, this represents a large
513 power consumption by the air blower for a long period of time (13.5 h). Therefore, the use of the controller is
514 advisable because it allows the reduction of otherwise dangerous local temperature gradients while avoiding
515 excessively high air flow rates for a long time. Furthermore, when the cell temperature gradient is controlled, the
516 thermal transitions, obtained by varying the air flow rate, were found to be small and are not expected to cause any
517 problem during the operation of the ReSOC. Hence, it is clear how the increased air flow rate, after a positive
518 change in the current density when working in exothermic mode, results in higher convective cooling of the cell,
519 thus maintaining the temperature within safe limits. When the average current density is reduced, in endothermic
520 operation, the drop of temperature can be decreased reducing the air flow. Near the thermoneutral operation, ∇T_{\max}
521 was only slightly influenced by the difference in the air flow, thus demonstrating that the control strategy does not
522 affect this operating mode. In fact, ∇T_{\max} near the thermoneutral operation is small (as illustrated later in Figure
523 13b), and the temperature of the solid structure is close to the stream temperature; thus, only a limited convective
524 heat transfer occurs. The farther the cell is from the thermoneutral operation, the more visible the effects of
525 manipulating the air are because the heat transfer between the solid structure and the air would be significant.

526
527 **Figure 7 Cell behavior with and without local temperature gradients controller. (a) The three cases investigated to illustrate the cell**
528 **behavior with or without the implementation of the PI controller: a constant, small air flow; a constant, large air flow; and a**
529 **manipulated air flow. (b) Maximum local solid structure temperature gradients against the average current density**

530
531 Figure 8 shows the comparison of the reactant utilization between a controlled and uncontrolled
532 operation/scenario. In the uncontrolled scenario, the maximum flow is chosen to have a U of 75% at a current
533 density of 6700 A/m². In the controlled operation, between -1500 and 1500 A/m², the fuel flow reaches the low
534 limit selected for the controller and therefore U varies. When U is not controlled and the fuel not manipulated,
535 with substantial changes in load, U might increase dramatically and the fuel can be completely depleted.
536 Furthermore, when considering to extend the study to the system level in the future, energy saving can be achieved
537 when U is controlled owing to the lower requirements in steam production and fuel processing.

538
539 **Figure 8 Reactant utilization (U) with and without PI controller, i.e., is with a variable fuel flow and constant fuel flow, respectively**

541 3.2.2 Detailed electrochemical and thermal ReSOC behavior under dynamic operation with controllers

542 The detailed electrochemical and thermal cell behavior under dynamic operation is illustrated in Figure 9. The
543 current density is ramped linearly in time (Figure 9a).

544 When operating the cell in SOEC mode, a decrease in the current density leads to a reduction in the operating
545 voltage and consequent decrease in electrical energy consumption, as depicted in Figure 9b. This will also result
546 in a lower production of H₂. In fuel cell mode, the rise in current density causes a decrease in cell voltage, which
547 leads to a larger waste heat production with the consequent temperature increase, shown in Figure 9c. The changes
548 caused by the transient operation have different response times, variations in voltage, and consequently, power
549 output, which are faster than the changes in temperature, as shown in Figure 9b and 9c. Dominated by
550 electrochemistry, the voltage could follow the changes in current density rapidly (in the order of few seconds), and
551 tended to stabilize instantaneously. During a decrease in the current density, an immediate drop in the irreversible
552 losses appears. Conversely, when the current density increases, the voltage rapidly decreases owing to the increase

553 in polarization. While the operating voltages are almost immediately reversed after the current density switched
554 between SOEC and SOFC modes, the temperature of the cell changed gradually owing to its thermal inertia (Figure
555 9c). At the end of the ramp, the cell temperature reaches its steady state at 3250 A/m² in approximately 18 min.

556 Figure 9c illustrates the temperature of the solid structure evaluated in the different control volumes of the cell
557 length (between the inlet and the outlet of the cell, control volume 1 and control volume 10 respectively) against
558 current density and time. It is evident in Figure 9c how the temperature profile in SOFC is steeper than in the
559 SOEC mode. In fact, the temperature outlet change (control volume 10) of the exothermic cell occurs in a faster
560 rate than that of the SOEC. Decreasing the average current density leads to a decrease in the heat generated via
561 irreversible losses, thus reducing the temperature of the cell. Conversely, after the switch between SOEC and
562 SOFC modes, the positive changes in the current density are followed by a rapid rise in the outlet temperature.
563 During the ramp, when the current density rises and the exothermicity of the fuel cell grows, the increase in the
564 air flow results in convective cooling of the cell. On the contrary, when the current density decreases, the air flow
565 diminishes to reduce its convective cooling. The lowest and highest temperatures of the solid structure, in SOEC
566 and SOFC modes, respectively, are observed at the cell outlet. The maximum temperature difference across the
567 solid structure of the cell length (between control volume 1 and control volume 10) is 62 °C, at 3211 A/m². After
568 the cell switches between SOEC and SOFC mode, the first volume of the cell undergoes a rise in temperature of
569 approximately 40 °C over a period of 1.2 h. A steeper increase in temperature (ΔT 130 °C) is observed in the last
570 volume of control over a period of 1.45 h. A “V” shape in the temperature profile is also observed in Figure 9c
571 (dashed oval). This might be related to a combination of two phenomena. The temperature drop is explained by
572 the impossibility to further reduce the air flow owing to the limits imposed in the controller, and the endothermic
573 behavior of the cell. Initially, the minimum air flow is not sufficient to balance the cell endothermicity.
574 Subsequently, when the endothermicity is no longer predominant, the temperature raises over the temperature of
575 the air stream. This phenomenon is more pronounced in the first volume of control, and it is also detectable in the
576 local temperature gradient transients profile, as presented in Figure 9d.

577 The controller is able to keep the local temperature gradients within the safe boundaries (Figure 9d). It is
578 interesting to notice that the highest temperature gradient is depicted toward the inlet of the cell (first control
579 volume) in both the fuel cell and electrolyzer operation. In the first control volume, the temperature gradient is
580 close to the limit of the safe operation region, while toward the outlet of the cell, under our operating conditions,
581 the local temperature gradients are way below the dangerous limit. Another aspect that deserves explanation is the
582 rapid increase in the temperature profiles of each control volume when the current density increases from 0 to 900
583 A/m². This is due to the local temperature gradients in every control volume. In fact, the controller only provides
584 the minimum air flow (as shown in Figure 7a) because the local temperature gradients are lower than the safe limit.
585 At 900 A/m², the maximum local temperature gradients reach the safe limit, and consequently, the controller starts
586 to provide a larger air flow to maintain them below the safe limit operation. From this point onwards, the controller
587 is able to keep a small variation in the temperature over the average current densities.

588 As shown in Figure 9e, the maximum ΔT in the SOEC is -65.2 °C for the fuel at 2383 A/m² and -60.9 °C for
589 air at 814 A/m². In the SOFC, the maximum ΔT results 83.8 °C for the fuel and 70.7 °C for the air, both at 3250
590 A/m². As shown in the figure, the thermal inertia of the SOC cell is evident. For a current density of 6640 A/m²,
591 which corresponds to thermoneutral current density, both gas streams have a positive ΔT . Moreover, only after
592 reducing the current density to 6200 A/m², the ΔT of fuel crosses the zero point, while for air the current density
593 needs to drop at 5400 A/m².

594 **Figure 9 Electrochemical and thermal cell behavior under dynamic operation when current density is ramped linearly in time,**
595 **switching between SOEC operation (6700 A/m²) to SOFC operation (3250 A/m²).** (a) Linear current density ramp in time. (b)
596 **Operating cell voltage, Nernst potential and thermoneutral voltage against current density and time. (c) Temperature of the solid**
597 **structure evaluated in the different control volumes of the cell length against current density and time. (d) Local temperature**
598 **gradients of the solid structure appraised in the different control volumes across the cell length versus current density and time. (e)**
599 **Temperature difference between the inlet and outlet of the fuel and air streams against current density and time**
600

601
602 We have seen before that the temperature affects the voltage (Nernst voltage and ASR decrease with increasing
603 temperature), but the voltage dependence on current density is predominant. To illustrate this dependence better,
604 Figure 10a shows the difference between the time sequential points for the voltage and its composing parts: Nernst
605 voltage, current density, and ASR. The plot covers the interval $5.69 \times 10^{-4} - 5.99 \times 10^{-4}$ s, corresponding to the
606 current density interval 3000 – 3250 A/m². Up to 5.775×10^{-4} s, that is, when the current reaches the constant
607 value of 3250 A/m², the voltage varies mostly owing to the change in current density and only to a negligible extent
608 to the variation in ASR and Nernst potential cause by the temperature change. When the current reaches the stable
609 value of 3250 A/m², the Nernst voltage shows a peak. This is due to the slight delay of the controller in adjusting
610 the fuel utilization, resulting in hydrogen excess. The negligible effect of temperature on voltage and the thermal
611 inertia effect are also visible in Figure 10b and Figure 10c, where the temperature and the voltage trends are
612 compared with that of the current density. While the voltage reaches an almost stable value quickly after the current
613 density arrives at the constant value of 3250 A/m², the temperature continues to decrease in the time interval in
614 analysis.

615
616 **Figure 10 Detailed analysis of the cell operating voltage between the ending part of the ramp at 3000 A/cm² and the steady-state at**
617 **3250 A/m² in SOFC mode, to show how it is differently affected by temperature and current density. (a) Difference between time**
618 **sequential points for the cell voltage and its contributors (Nernst voltage, current density, and ASR) and H₂ utilization to correlate**
619 **with Nernst Potential gradient. (b) Temperature variation as a correlation variable for ASR and Nernst potential gradients. (c)**
620 **Operating cell voltage variation against time and current density**

621 3.2.3 Dynamic behavior of ReSOC under transient operation, with controllers at different current ramps

622 Additional simulations are run to evaluate the response of the cell under different values of the current ramp,
623 which is now doubled and halved to the initial nominal set-point. Commonly, the multi-loop controllers are tuned
624 for nominal operating conditions and may start exhibiting unstable behavior under different operating conditions.
625 The cell is controlled by the same controllers as before. The results are detailed in Figure 11 and Figure 12.

626 **Figure 11 Reactant utilization with ramps of 1A/min , 0.25A/min, and 0.5 A/min**

627
628
629 The simulations show that the reactant utilization controller, which manipulates the fuel flow rates through the
630 cell, is able to keep U of 75% for all the different ramp rates, thus avoiding fuel starvation owing to rapid
631 consumption of the reactants (Figure 11).

632
633 **Figure 12 Maximum local temperature gradients when the cell undergoes different current ramp rates from 6700 A/m² to 3250**
634 **A/m². (a) Air mass flow variation. (b) Maximum local temperature gradients for the different ramp rates**

635
636 The temperature control strategy is able to keep the cell maximum local temperature gradients within their
637 safety limits, even with a ramp of 1 A/min (Figure 12a-12b). The controller, tuned for a ramp of 0.5 A/min, is
638 therefore capable of successfully handle the additional ramps investigated without exhibiting unstable behavior.

639 3.2.4 Electrochemical and thermal parameters distribution along the ReSOC length, in SOEC and SOFC 640 steady-state operations

641 The results of the steady-state analysis are depicted in Figure 13.

642
643 **Figure 13 Electrochemical and thermal parameter distribution along the cell length, for three average current densities: 6700 A/m²**
644 **(SOEC mode, slightly exothermic behavior), 5000 A/m² (SOEC mode, endothermic behavior), and 3250 A/m² (SOFC mode,**
645 **exothermic behavior). (a) Local temperature gradients. (b) Solid structure temperature profile. (c) Nernst potential, operating cell**
646 **voltage and thermoneutral voltage profiles. (d) ASR profile. (e) Local current density distributions**

647
648 Local temperature gradients depend on the average current densities (Figure 13a), and thus they demand for a
649 local cell temperature control. The influence of the average current densities on the local temperature gradients is
650 related to the heat produced by the irreversible losses within the cell and the one produced or consumed by the
651 exothermic or endothermic reactions (TAS). In SOEC operation, the ∇T_{\max} is below 6 °C; therefore, the controller
652 provides only the minimum air flow rate defined as its limit. When working in SOFC mode, the excess of heat
653 produced through the irreversible losses causes the temperature to rise, as depicted in Figure 13b. In SOEC mode
654 at 5000 A/m², the irreversible losses do not provide enough heat to cover the amount consumed by the reaction,
655 and the SOEC temperature decreases along the cell, as shown in Figure 13b. In SOFC operation at 3250 A/m², the
656 heat accumulated leads to an increase in temperature toward the outlet of the cell.

657 For the exothermic cell, at 3250 A/m², a greater change in the solid temperature was depicted. The total
658 temperature difference along the cell is 61.5 °C at 3250 A/m², -4.5°C at 6700 A/m², and -35.4 °C at 5000 A/m²,
659 (Figure 13b). As shown in the figure, even when the SOEC is globally endothermic (5000 A/m²) in the firsts four
660 volumes its solid-structure temperature is higher than 750 °C. Owing to thermal inertia, the solid structure needs
661 time to cool and transfer the heat to the gas stream. The temperature decreases below 750 °C just before the middle
662 of the cell. The inlet solid structure temperature corresponds to the highest temperature in the SOEC when working
663 endothermically and to the lowest temperature in the SOFC. The air flow originates convective heat transfer with
664 the solid structure supplying cooling and heating to the SOFC and SOEC cells, respectively. The negative and
665 positive temperature difference along the cell in endothermic and exothermic modes decreases or increases toward
666 the outlet, respectively.

667 The SOFC voltage at 3250 A/m² is 0.774 V while the SOEC voltage at 5000 A/m² is 1.269 V, (Figure 13c). In
668 the SOEC, at 6700 A/m² and 1.29 V, the temperature does not vary largely (∇T_{\max} below 1 °C) because the cell is
669 working close to its thermoneutral point (1.288 V) where the heat produced by the irreversible losses matches that
670 consumed by the electrochemical reaction (Figure 13a, 13b and 13c).

671 As presented in Figure 13c, the Nernst potential trend is proportional to the temperature distribution and gas
672 concentration along the cell. In the SOFC case, the thermodynamics predicts the Nernst potential to reduce as the
673 temperature increases, the reactants reduce, and the products rise along the cell. Conversely, when the cell is
674 working at -5000 A/m² as electrolyzer, its temperature decreases, the reactants increase, and the products decrease
675 over the cell length; therefore, the Nernst potential slightly increases. When working in the SOEC mode at 6700

676 A/m^2 , the Nernst potential increases even if its solid temperature is almost stable along the cell. This shows that
677 the impact of the change in gas composition is higher than that of cell temperature under this condition.

678 The ASR trend is inversely proportionally to that of the cell temperature; thus, in the SOFC the resistance
679 decreases along the cell length while in the SOEC it increases toward the outlet of the cell (Figure 13d). The local
680 current density distributions along the cell length are shown in Figure 13e for all the average current densities. The
681 current densities decrease along the cell length in both operational modes. Consequently, considering a current
682 efficiency of 100%, the H_2 and the O_2 production or consumption rates also decrease along the cell as well. In the
683 same figure, it is interesting to notice that the exothermic SOFC shows the greatest local current density decrease
684 near the outlet of the cell, while when working in SOEC mode, the greatest drop is toward the inlet, with an
685 accentuated behavior at $5000 A/m^2$. When operating endothermically, in SOEC mode at $5000 A/m^2$, the change in
686 the stream composition and the negative ∇T_{max} synergistically contribute to the decrease in local current density
687 toward the outlet. In SOEC mode at $6700 A/m^2$, the change in stream composition prevails on the small ∇T_{max} ,
688 inducing the decrease in the local current density along the cell.

689 4 Conclusion

690 The ReSOC system can be used in both fuel cell and electrolyzer modes, thus serving as an electricity storage
691 and production technology. Temperature and reactant utilization control are crucial during transient operation to
692 avoid fuel starvation and minimize temperature variation, thus preventing thermo-mechanical stress that might
693 lead to component fracture or degradation. This study is a first step in the dynamic analysis of a reversible stack
694 switching between SOFC and SOEC modes. The stack transient response and control under a varying load are
695 presented to demonstrate the success of the designed control strategy. Two 1D dynamic models of SOCs are built
696 and compared with those in the literature. After having evaluated the safe stack operating ranges, the SOFC and
697 SOEC models are used to study the steady-state and dynamic behavior of these stacks, along with the prospect for
698 local stack temperature gradient and fuel utilization control through variation of the air and fuel flow rates. The
699 stacks appeared stable and controllable with two PI controllers, without need for more aggressive or expensive
700 control strategies.

701 Furthermore, the two models have been integrated to simulate the ReSOC response to transient operation. The
702 same controllers are used to maintain safe stack operating conditions. The results show that both the
703 electrochemical and heat transfer greatly influence the transient process, but on different time scales. The voltage
704 transient owing to load changes responds within few seconds, while the temperature transient requires a longer
705 time. The controllers are capable of bringing the reactant utilization to the desired value in 50 s while it takes
706 almost 10 min for the local temperature gradient to reach its set-point.

707 The steady-state simulation showed that the cell performance is greatly affected by the solid-structure
708 temperature and the operating current density. The selection of operating conditions for a ReSOC (e.g., current
709 density and temperature) largely affects the irreversible losses, thus influencing the cell voltage.

710 The changes in the average current density cause the stack temperature to vary during both exothermic and
711 endothermic operations, thus calling for temperature control, particularly in dynamic operation. The results
712 illustrate that, even if the cell solid-structure temperature is altered via changes in the average current density, the
713 proposed control strategy is able to keep the overall temperature difference and the maximum local temperature
714 gradient in the solid structure within safe bounds for both the endothermic and exothermic operation modes, and
715 this leads to an almost stable temperature even in dynamic operation. The control strategy does not affect operation
716 near thermoneutral operation; in fact, the local temperature gradients are only slightly influenced by the controller.

717 After switching from SOEC to SOFC mode, the stack temperature reaches its steady state at $3250 A/m^2$ in
718 approximately 18 min. The maximum temperature difference across the solid structure of the cell length is $62 ^\circ C$
719 at $3211 A/m^2$. The maximum fuel channel ΔT ($-65.2 ^\circ C$) in the SOEC is reached at $2383 A/m^2$, and at $814 A/m^2$
720 for the air channel ($60.9 ^\circ C$). In the SOFC, the ΔT for the fuel is $83.8 ^\circ C$ and $70.7 ^\circ C$, both at $3250 A/m^2$. The
721 dynamic response of the cell temperature is mainly governed by thermal inertia. When operating at thermoneutral
722 current density ($6640 A/m^2$), both gas streams have a positive ΔT , and the fuel ΔT crosses the zero point only after
723 reducing the current density to $6200 A/m^2$. The current density needs to drop to $5400 A/m^2$ for the air to cross the
724 zero point.

725 Without a controller, the operation of the ReSOC within safe operating limits might not be assured for a low
726 air flow rate. The temperature local gradients are kept under safe bounds by manipulating the air flow rate. Such
727 a control strategy shows good potential to prevent the issues of cell-component fracture owing to temperature
728 fluctuations during dynamic operation. Moreover, considering to extend the study to the system level in the future,
729 this might reduce the large power consumption that would be required by the air blower to keep the stack within
730 the safe operation limits in the case of an uncontrolled operation. Energy saving can also be achieved when the
731 reactant utilization is controlled owing to the lower requirement of steam production.

732 The same controllers are able to maintain the reactant utilization at the desired value and the maximum local
733 temperature gradients of the solid structure, under different current ramp rates.

734 The dynamic behavior of the stack through its transfer function has been studied and the parameters of a PI
735 controller have been determined; an actual PLC can therefore be programmed to control the ReSOC. The main
736 dynamic properties of the ReSOC are captured. Furthermore, the results offer successful control strategies for the
737 selected conditions and provide a good starting point for identifying the optimal control strategy in real-world
738 applications. The study should be extended to a whole system (including BoP) to assess its response to a dynamic
739 operation.

740 **Acknowledgment**

741

742 The authors acknowledge Prof. Casella for the useful discussion on Modelica language and the use of
743 *Dymola* software.

Reference

- 744
745
746
747 [1] P. Mottaghizadeh, et al. Process modeling of a reversible solid oxide cell (r-SOC) energy storage system
748 utilizing commercially available SOC reactor. *Energy conversion and management* 142 (2017).
- 749 [2] A. Buttler, S. Hartmut. Current status of water electrolysis for energy storage, grid balancing and sector
750 coupling via power-to-gas and power-to-liquids: A review. *Renewable and Sustainable Energy Reviews*. (2017).
- 751 [3] P. Aguiar, C.S. Adjiman, N.P. Brandon. Anode-supported intermediate-temperature direct internal reforming
752 solid oxide fuel cell: Model-based dynamic performance and control. *Journal of Power Sources*. 147 (2005) 136-
753 47.
- 754 [4] B. Huang, Y. Qi, M. Murshed. Solid oxide fuel cell: Perspective of dynamic modeling and control. *Journal of*
755 *Process Control* 21 (2011) 1426-37.
- 756 [5] J.S. Szmyd, Y. Komatsu, G. Brus, F. Ghigliazza, S. Kimijima, A. Sciazko. The effect of applied control strategy
757 on the current-voltage correlation of a solid oxide fuel cell stack during dynamic operation. *archives of*
758 *thermodynamics*. 35 (2014) 129-43.
- 759 [6] J. Kupecki, J. Milewski, A. Szczesniak, R. Bernat, K. Motylinski. Dynamic numerical analysis of cross-, co-
760 -, and counter-current flow configuration of a 1 kW-class solid oxide fuel cell stack. *Hydrogen Energy*. 40 (2015)
761 15834-44.
- 762 [7] J. Kupecki, K. Motylinski, J. Milewski. Dynamic Modelling of the Direct Internal Reforming (DIR) of Methane
763 in 60-cell Stack with Electrolyte Supported Cells. 105 (2017) 1700-5.
- 764 [8] J. Kupecki, K. Motylinski, J. Milewski. Dynamic analysis of direct internal reforming in a SOFC stack with
765 electrolyte-supported cells using a quasi-1D model. *Applied Energy*
- 766 [9] T. Ota, M. Koyama, C. Wen, K. Yamada, H. Takahashi. Object-based modeling of SOFC system: dynamic
767 behaviour of micro-tube SOFC. *J Power Sources*. 118 (2003) 430-9.
- 768 [10] E. Achenbach. Responses of a solid oxide fuel cell to load changes *J Power Sources*. 57 (1995) 105-9.
- 769 [11] P. Aguiar, C.S. Adjiman, N.P. Brandon. Anode-supported intermediate-temperature direct internal reforming
770 solid oxide fuel cell: model-based steady-state performance. *J Power Sources*. 138 (2004) 120-36.
- 771 [12] S. Kourosch, A. Feliachi. Dynamic and Transient Analysis of Power Distribution Systems With Fuel Cells-Part
772 I: Fuel- Cell Dynamic Model. *IEEE transactions on energy conversion*. 19 (2004).
- 773 [13] P. Pianko-Oprych, S.M. Hosseini. Dynamic Analysis of Load Operations of Two-Stage SOFC stacks Power
774 Generation System. *Energies*. 10 (2017).
- 775 [14] A. Chaisantikulwat, C. Diaz-Goano, E.S. Meadows. Dynamic modelling and control of planar anode-
776 supported solid oxide fuel cell. *Computers & Chemical Engineering*. 32 (2008) 2365-81.
- 777 [15] F. Mueller, J. Brouwer, F. Jabbari, S. Samuelsen. Dynamic Simulation of an Integrated Solid Oxide Fuel Cell
778 System Including Current-Based Fuel Flow Control. *ASME J Fuel Cell Sci Technol*. 3 (2006) 144-54.
- 779 [16] D.F. Cheddie, N.D.H. Munroe. A dynamic 1D model of a solid oxide fuel cell for real time simulation. *Journal*
780 *of Power Sources*. 171 (2007) 634-43.
- 781 [17] S. Lee, H. Kim, K.J. Yoon, J.W. Son, J.H. Lee, B.K. Kim, et al. The effect of fuel utilization on heat and mass
782 transfer within solid oxide fuel cells examined by three-dimensional numerical simulations. *International Journal*
783 *of Heat and Mass Transfer*. 97 (2016) 77-93.
- 784 [18] Y. Bae, S. Lee, K.J. Yoon, J.H. Lee, J. Hong. Three-dimensional dynamic modeling and transport analysis of
785 solid oxide fuel cells under electrical load change. *Energy Conversion and Management*. 165 (2018) 405-18.
- 786 [19] M. Sorrentino, C. Pianese. Model-based development of low-level control strategies for transient operation
787 of solid oxide fuel cell systems. *Journal of Power Sources*. 196 (2011) 9036-45.
- 788 [20] M. Sorrentino, D. Marra, C. Pianese, M. Guida, F. Postiglione, K. Wang, et al. On the Use of Neural Networks
789 and Statistical Tools for Nonlinear Modeling and On-field Diagnosis of Solid Oxide Fuel Cell Stacks. *Energy*
790 *Procedia*. 45 (2014) 298-307.
- 791 [21] M. Gallo, D. Marra, M. Sorrentino, C. Pianese, S. Fai. Development of a Dynamic Model for Diagnosis and
792 Control of an Integrated Stack Module Based on Solid Oxide Fuel Cells. *Energy Procedia* 105 (2017) 1936-41.
- 793 [22] D. Marra, M. Sorrentino, A. Pohjoranta, C. Pianese, J. Kiviahho. A lumped dynamic modelling approach for
794 model-based control and diagnosis of solid oxide fuel cell system with anode off-gas recycling. . *ECS Transactions*.
795 68 (2015) 3095-106.
- 796 [23] J. K.K., S.J. Andreasen, H.R. Shaker. Dynamic modelling of a reformed methanol fuel cell system using
797 empirical data and adaptive neuro-fuzzy inference system models. . *Journal of Fuel Cell Science and Technology*.
798 11 (2014).
- 799 [24] R.A. Roberts, J. Brouwer. Dynamic simulation of a 220 kW solid oxide fuel cell gas turbine hybrid system
800 with comparison to data. *ASME J Fuel Cell Sci Technol*. 3 (2006) 18-25.

801 [25] T. Kaneko, J. Brouwer, G.S. Samuelsen. Power and temperature control of fluctuating biomass gas fueled
802 solid oxide fuel cell and micro gas turbine hybrid system. *Journal of Power Sources*. 160 (2006) 316-25.

803 [26] R.A. Roberts, J. Brouwer, F. Jabbari, et, al. Control design of an atmospheric solid oxide fuel cell/gas turbine
804 system: variable versus fixed speed gas turbine operation. *Journal of Power Sources*. 161 (2006) 484-91.

805 [27] F. Mueller, J. Brouwer, S.G. Kang. Quasi-three dimensional dynamic model of a proton exchange membrane
806 fuel cell for system and controls development. *Journal of Power Sources*. 163 (2007) 814-29.

807 [28] F. Mueller, R.M. Gaynor, A.E. Auld, a.l. et. Synergistic integration of gas turbine and solid oxide fuel cell for
808 improved transient capability. *Journal of Power Sources*. 176 (2008) 229-39.

809 [29] R.M. Gaynor, F. Mueller, F. Jabbari, et al. On control concepts to prevent fuel starvation in solid oxide fuel
810 cells. *Journal of Power Sources*. 180 (2008) 330-42.

811 [30] F. Mueller, F. Jabbari, J. Brouwer, et al. On the intrinsic transient capability and limitations of solid oxide fuel
812 cell systems. *Journal of Power Sources*. 187 (2009) 452-60.

813 [31] D. McLarty, Y. Kuniba, J. Brouwer. Experimental and theoretical evidence for control requirements in solid
814 oxide fuel cell gas turbine hybrid systems *Journal of Power Sources*. 209 (2012) 195-203

815 [32] D. McLarty, J. Brouwer, G.S. Samuelsen. A spatially resolved physical model for transient system analysis of
816 high temperature fuel cells. *Int J Hydrogen Energ*. 38 (2013) 7935-46.

817 [33] D. McLarty, J. Brouwer, G.S. Samuelsen. Fuel cell-gas turbine hybrid system design part II: dynamics and
818 control *Journal of Power Sources*. 254 (2014) 126-36.

819 [34] D. McLarty, J. Brouwer. A poly-generating closed cathode fuel cell with carbon capture. *Appl Energy*. 131
820 (2014) 108-13.

821 [35] D. McLarty, J. Brouwer. Micro-grid energy dispatch optimization and predictive control algorithms; A UC
822 Irvine case study. *Int J Electrical Power Eng Sys* 65 (2015) 179-90.

823 [36] J. Brouwer, D. McLarty, R. Roberts. Chapter 6, System Dynamics and Control. in: J. Kupecki, (Ed.).
824 Modeling, Design, Construction, and Operation of Power Generators with Solid Oxide Fuel Cells From Single
825 Cell to Complete Power System Springer 2018.

826 [37] A. Pohjoranta, M. Halinen, J. Pennanen, J. Kiviaho. Solid oxide fuel cell stack temperature estimation with
827 data-based modeling – Designed experiments and parameter identification. *Journal of Power Sources*. 277 (2015)
828 464-73.

829 [38] P. Leone, A. Lanzini. Experimental Modeling of Transients in Large SOFC Systems. *J Fuel Cell Sci Technol*
830 10 (2013).

831 [39] L. Barelli, G. Bidini, A. Ottaviano. Solid oxide fuel cell: Electrochemical performance and thermal
832 management during load-following operation. *Energy*. 115 (2016) 107-19.

833 [40] E.F. Tchonla. SOFC-Brennstoffzellen-Kraftwerke für die dezentrale elektrische Energieversorgung. .
834 Erlangen, 2012.

835 [41] Y. Luo, Y. Shi, Y. Zheng, N. Cai. Reversible solid oxide fuel cell for natural gas/renewable hybrid power
836 generation systems. *Journal of Power Sources*. 340 (2017) 60-70.

837 [42] S. Wahl, A.G. Segarra, P. Horstmann, M. Carre, W.G. Bessler, F. Lapique, et al. Modeling of a thermally
838 integrated 10 kWe planar solid oxide fuel cell system with anode offgas recycling and internal reforming by
839 discretization in flow direction. . *Journal of Power Sources*. 279 (2015) 656-66.

840 [43] M. Windeknecht, P. Tzscheuschler. Optimization of the heat output of high temperature fuel cell micro-CHP
841 in single family homes. in: IABP, (Ed.). 6th International Building Physics Conference (IBPC) 2015.

842 [44] Y. Luo, Y. Shi, W. Li, N. Cai. Dynamic electro-thermal modeling of co-electrolysis of steam and carbon
843 dioxide in a tubular solid oxide electrolysis cell. *Energy - Elsevier*. 89 (2015) 637-47.

844 [45] P. Aguiar, N.P. Brandon, J. Udagawa. Hydrogen production through steam electrolysis: Model-based dynamic
845 behaviour of a cathode-supported intermediate temperature solid oxide electrolysis cell. *Journal of Power Sources*.
846 180 (2008) 46-88.

847 [46] J. Udagawa, P. Aguiar, N.P. Brandon. Hydrogen production through steam electrolysis: Model-based dynamic
848 behaviour of a cathode-supported intermediate temperature solid oxide electrolysis cell *Journal of Power Sources*.
849 180 (2008) 46-55.

850 [47] Q. Cai, N.P. Brandon, C.S. Adjiman. Modelling the dynamic response of a solid oxide steam electrolyser to
851 transient inputs during renewable hydrogen production. *Front Energy Power Eng China*. 4 (2010) 211-22.

852 [48] J. Udagawa, P. Aguiar, N. Brandon. Hydrogen production through steam electrolysis: control strategies for a
853 cathode-supported intermediate temperature solid oxide electrolysis cell *Journal of Power Sources*. 180 (2008)
854 354-64.

855 [49] Q. Cai, A.W.V. Haw, C.S. Adjiman, N.P. Brandon. Hydrogen production through steam electrolysis: a model-
856 based study. in: Ian David Lockhart Bogle and Michael Fairweather, B.V. Elsevier, (Eds.), 22nd European
857 Symposium on Computer Aided Process Engineering, London, 17 - 20 June 2012.

858 [50] C.H. Wendel, P. Kazempoor, R.J. Braun. Novel electrical energy storage system based on reversible solid
859 oxide cells: System design and operating conditions. *J Power Sources*. 276 (2015) 133-44.

860 [51] X. Zhang, S.H. Chan, H.K. Ho, M. Li, G. Li, J. Li, et al. Towards a smart energy network: the roles of
861 fuel/electrolysis cells and technological perspectives. *Int J Hydrogen Energy*. 40 (2015) 6866-919.

862 [52] A. Atkinson, A. Selcuk. Mechanical behaviour of ceramic oxygen ion-conducting membranes. *Solid State*
863 *Ionics*. 134 (2000) 59-66.

864 [53] P. Di Giorgio, U. Desideri. Potential of Reversible Solid Oxide Cells as Electrical Storage System. *Energies*.
865 9 (2016).

866 [54] P. Kazempoor, R.J. Braun. Model validation and performance analysis of regenerative solid oxide cells for
867 energy storage applications: reversible operation. *Int J Hydrogen Energy*. 39 (2015).

868 [55] C.H. Wendel. Design and analysis of reversible solid oxide cell systems for electrical energy storage. Colorado
869 Schools of Mines 2015.

870 [56] C.H. Wendel, Z. Gao, S.A. Bennett, R.J. Braun. Modeling and experimental performance of an intermediate
871 temperature reversible solid oxide cell for high-efficiency, distributed-scale electrical energy storage. *J Power*
872 *Sources*. 283 (2015) 329-42.

873 [57] C.H. Wendel, R.J. Braun. Design and techno-economic analysis of a high efficiency reversible solid oxide cell
874 systems for distributed energy storage. *Applied Energy*. 172 (2016) 118-31.

875 [58] C.H. Wendel, P. Kazempoor, R.J. Braun. A thermodynamic approach for selecting operating conditions in the
876 design of reversible solid oxide cell energy systems. *Journal of Power Sources*. 301 (2015).

877 [59] D. Klotz, A. Leonide, A. Weber, E. Ivers-Tiffée. Electrochemical model for SOFC and SOEC mode predicting
878 performance and efficiency. *J Hydrogen Energy*. 39 (2014) 20844-9.

879 [60] D. Ferrero, A. Lanzini, P. Leone, M. Santarelli. Reversible operation of solid oxide cells under electrolysis
880 and fuel cell modes: Experimental study and model validation. *Chemical Engineering Journal*. 274 (2015) 143-55.

881 [61] V.N. Nguyen, Q. Fang, U. Packbier, L. Blum. Long-term tests of a Julich planar short stack with reversible
882 solid oxide cells in both fuel cell and electrolysis modes. *Int J Hydrogen Energy*. 38 (2013) 4281-90.

883 [62] J. Sar, J. Schefold, A. Brisse, E. Djurado. Durability test on coral $Ce_{0.9}Gd_{0.1}O_{2-\delta}-La_{0.6}Sr_{0.4}Co_{0.2}Fe_{0.8}O_{3-\delta}$ with
884 $La_{0.6}Sr_{0.4}Co_{0.2}Fe_{0.8}O_{3-\delta}$ current collector working in SOFC and SOEC modes. *Electrochem Acta*. 201 (2016).

885 [63] J. Sanz-Bermejo, J. Muñoz-Anton, J. Gonzalez-Aguilar, M. Romero. Part load operation of a solid oxide
886 electrolysis cell. *International Journal of Hydrogen Energy*. 40 (2015) 8291-303.

887 [64] F. Petipas, A. Brisse, C. Bouallou. Modelled behaviour of a high temperature electrolyser system coupled
888 with a solar farm. *Chemical Engineering Transactions*,. (2015) 1015-20.

889 [65] F. Petipas, Q. Fu, A. Brisse, C. Bouallou. Transient operation of a solid oxide electrolysis cell. *International*
890 *Journal of Hydrogen Energy*. 37 (2013) 2957-64.

891 [66] F. Petipas, A. Brisse, C. Bouallou. Model-based behaviour of a high temperature electrolyser system operated
892 at various loads. *Journal of Power Sources*. 239 (2013).

893 [67] T. Strohbach, F. Mittmann, C. Walter, D. Schmanke. Sunfire Industrial SOC Stacks and Modules. *ECS*
894 *transactions* 68 (2015) 125-9.

895 [68] C. Graves, S. Ebbesen, S. Jensen, S. Simonsen, M. Mogensen. Eliminating degradation in solid oxide
896 electrochemical cells by reversible operation. *Nature Materials*. 14 (2015) 239-44.

897 [69] Y. Zheng, Y. Luo, Y. Shi, N. Cai. Dynamic Process of Switching in Reversible Solid Oxide Fuel Cells. *Journal*
898 *of Energy Engineering, (C) ASCE*. (2017).

899 [70] X. Jin, X. Xue. Mathematical modelling analysis of regenerative solid oxide fuel cells in switching mode
900 conditions. *Journal of Power Source*. 195 (2010) 6652-8.

901 [71] R. Ma, F. Gao, E. Breaz. Multi-Dimensional Reversible Solid Oxide Fuel Cell Modelling for Embedded
902 Applications. *IEEE Transactions on Energy Conversion* 33 (2018) 692 - 701.

903 [72] H. Er-rbib, N. Kezibri, C. Bouallaou. Dynamic simulation of Reversible Solid Oxide Cell (ReSOC) *Chemical*
904 *Engineering Transactions*. 61 (2017) 1075-80.

905 [73] H. Severson, M. Assadi. Analysis of residual and operational thermal stresses in a planar SOFC. *Journal of*
906 *Fueller Cell Science and Technology*. 10 (2013).

907 [74] S.E. Mattsson, H. Elmqvist, M. Otter. Physical system modeling with modelica. *Control Engineering Practice*.
908 6 (1998).

909 [75] Modelica™-Modelon. Fuel Cell Library.

910 [76] J. Udagawa, C.S. Adjiman, N.P. Brandon. Hydrogen production through steam electrolysis: Model-based
911 steady state performance of a cathode-supported intermediate temperature solid oxide electrolysis cell. *Journal*
912 *Power Sources*. 166 (2007) 127-36.

913 [77] D. Andersson, E. Åberg, J. Eborn. Dynamic modeling of a solid oxide fuel cell system in Modelica. 8th
914 Modelica Conference, Dresden, Germany, 2011.

915 [78] M. Hauck, S. Herrmann, H. Spliethoff. Simulation of a reversible SOFC with Aspen Plus. *Int J Hydrogen*
916 *Energy*. 42 (2017).

917 [79] D.M. Bierschenk, J.R. Wilson, S.A. Barnett. High efficiency electrical energy storage using methane-oxygen
918 solid oxide cell. *Energy Environ Sci*. 4 (2011).

919 [80] Z. Zhan, W. Kobsiriphat, J.R. Wilson, M. Pillai, I. Kim, S.A. Barnett. Syngas Production By Coelectrolysis
920 of CO₂/H₂O: The Basis for a Renewable Energy Cycle. *Energy & Fuels* 23 (2009) 3089-96.
921 [81] Q. Cai, C.S. Adjiman, N.P. Brandon. Optimal control strategies for hydrogen production when coupling solid
922 oxide electrolyzers with intermittent renewables energies. *Journal of Power Sources*. 268 (2014) 212-24.
923 [82] S.D. Ebbesen, R. Knibbe, M. Mogensen. Co-electrolysis of steam and carbon dioxide in solid oxide cells.
924 *Journal of The Electrochemical Society*. 159 (2012) 482-9.
925 [83] R.T. Leah, N.P. Brandon, P. Aguiar. Modelling of cells, stacks and systems based around metal-supported
926 planar IT-SOFC cells with CGO electrolytes operating at 500-600 °C. *Journal of Power Sources*. 145 (2005) 336-
927 52.
928 [84] Jensen SH, Graves C, Mogensen M, Wendel C, Braun R, Hughes G, et al. Large-scale electricity storage
929 utilizing reversible solid oxide cells combined with underground storage of CO₂ and CH₄. *Energy Environ Sci*
930 8(2015) 2471-9.
931 [85] N. Perdikaris, K.D. Panopoulos, P.H. Hofmann, S. Spyrikis, E. HKakaras. Design and exergetic analysis of a
932 novel carbon free tri-generation system for hydrogen, power and heat production from natural gas, based on
933 combined solid oxide fuel and electrolyser cells. *Journal of Hydrogen Energy*. 35 (2010) 2446-56.
934 [86] G.A. Whyatt, L.A. Chick. Electrical generation for more-electric aircraft using solid oxide fuel cells. U.S.
935 Department of Energy 2012.
936 [87] D.S. Modelon AB. <http://www.modelon.com/products/modelica-libraries/fuel-cell-library/>.
937 [88] S. Skogestad. *Multivariable Feedback Control: Analysis and Design*. Springer 1996.
938 [89] P. Bolzern, R. Scattolini, N. Schiavoni. *Fondamenti di controlli automatici*. McGraw-Hill Companies 2015.
939 [90] N. Chatrattanawet, S. Skogestad, A. Arpornwichanop. Control structure design and dynamic modeling for a
940 solid oxide fuel cell with direct internal reforming of methane. *Chemical Engineering Research and Design*. 98
941 (2015) 202-11.
942

Appendix A_ G(s) step response analysis.

Figure A. 1 a) SOEC case, temperature gradient and fuel utilization trends against a 1% inlet air flow step. b) SOFC case, temperature gradient and fuel utilization trends against a 1% inlet air flow step. c) SOEC case, temperature gradient and fuel utilization trends against a 1% inlet fuel flow step. d) SOFC case, temperature gradient and fuel utilization trends against a 1% inlet fuel flow step

According to the control theory, the diagonal transfer functions of a MIMO control system can be considered decoupled when a small variation of each one of the inputs has a considerable effect on the desired controlled variable (e.g., air mass flow and temperature gradient), and a less significant influence on the other(s) output(s). From a numerical point of view, the “measure” of the decoupling is given by the RGA matrix: the closer it is to the identity matrix, the more decoupled the system is. From a simulation point of view, the same result can be achieved by applying a small step variation on the inputs (around 1% to remain within the system linearity hypothesis) and checking how the outputs react once the transients are finished. Note this is a process transfer function G(s) property, and it does not involve the controllers by any means.

The four figures above show the trend of the outputs, namely, temperature gradient and reactant utilization, when a small step on the inputs, namely, air and fuel mass flows, is applied on the system. In particular,

- Figures A.1 a) and b): For both the SOEC and SOFC stacks operating under the inlet condition presented in Table A.1, a 1% negative step in the air mass flow is applied on the system at equilibrium. It is clear that the reactant utilization is constant, whereas the temperature gradient moves according to its dynamic (the SOFC dynamic is faster than that of the SOEC).

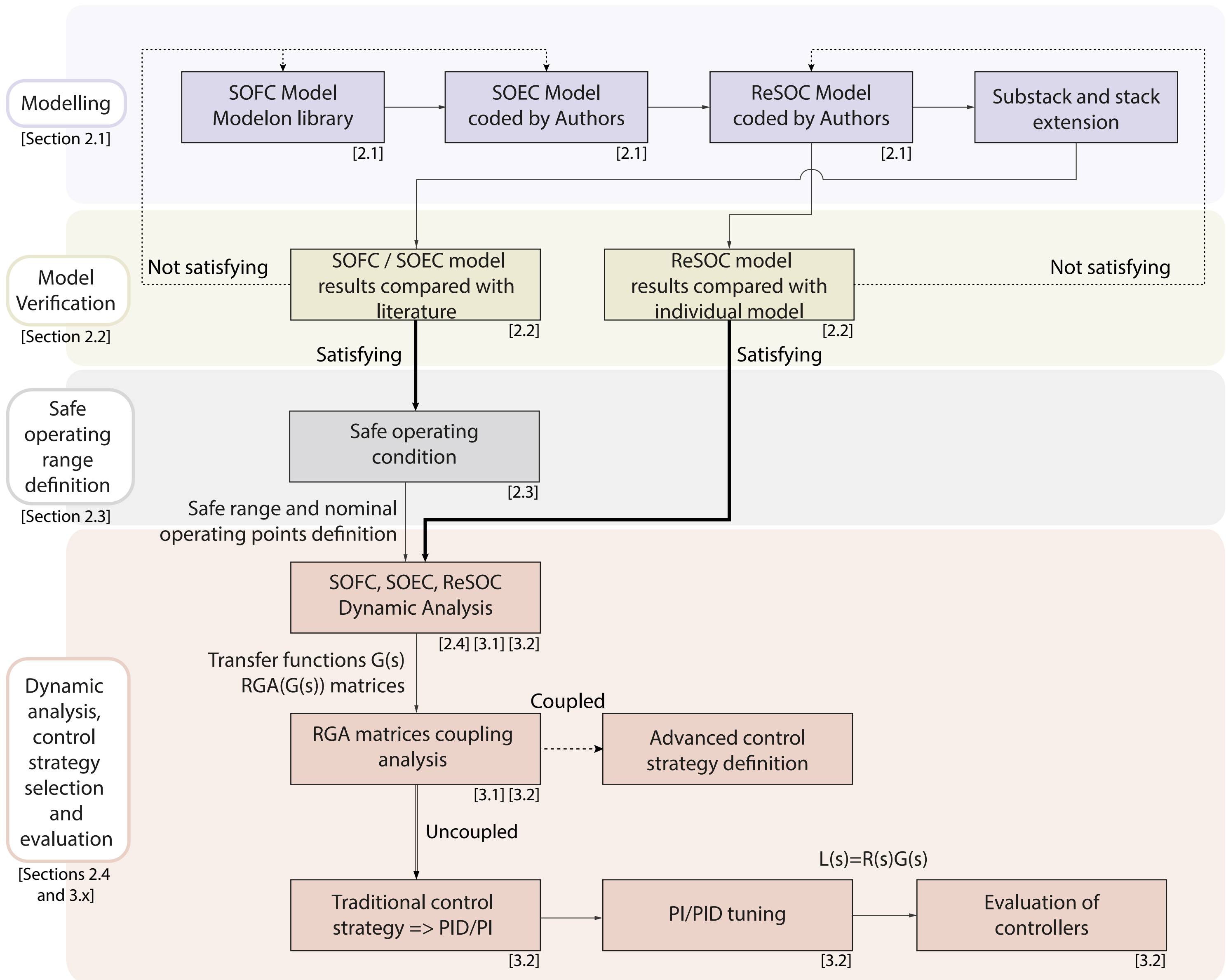
- Figures A.1 c) and d): For both the SOEC and SOFC stacks operating under the inlet condition presented in Table A.1, a 1% negative step in the fuel mass flow is applied on the system at equilibrium. In this case, the fuel variation has an effect on both outputs because the fuel also acts as a coolant/heating medium for the stack. However, its influence is more significant on the reactant utilization. In fact, if we evaluate the percentage shifts, a 1% variation in fuel causes only a 0.14% and 0.2% variation in local temperature gradients, and a 1.17% and 1.00% variation in reactant utilization. The difference of almost one order of magnitude between the two cases indicates that the effect of the fuel mass flow is much stronger on the reactant utilization than on the temperature gradient. Regarding the dynamics, the temperature gradient moves similarly to the air step cases, while the reactant utilization shows an undershoot.

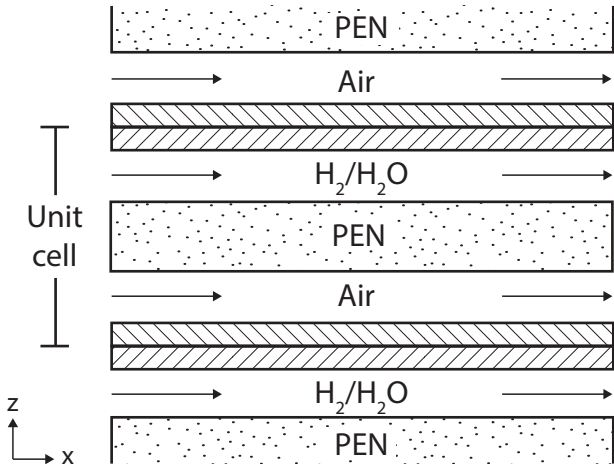
It is important to underline that the conclusion that the control system is decoupled is based on the static gains of the transfer functions. For instance, this means that when an input variation is applied to the process, both outputs can move dynamically but once the transient is finished (i.e. in static conditions) only the output related to the changed input shows a non-zero gain, while the other goes back to its previous value. The physical drivers behind this result could be different from those driving the dynamic of the process in terms of under/overshoots and settling time, since it is a static property.

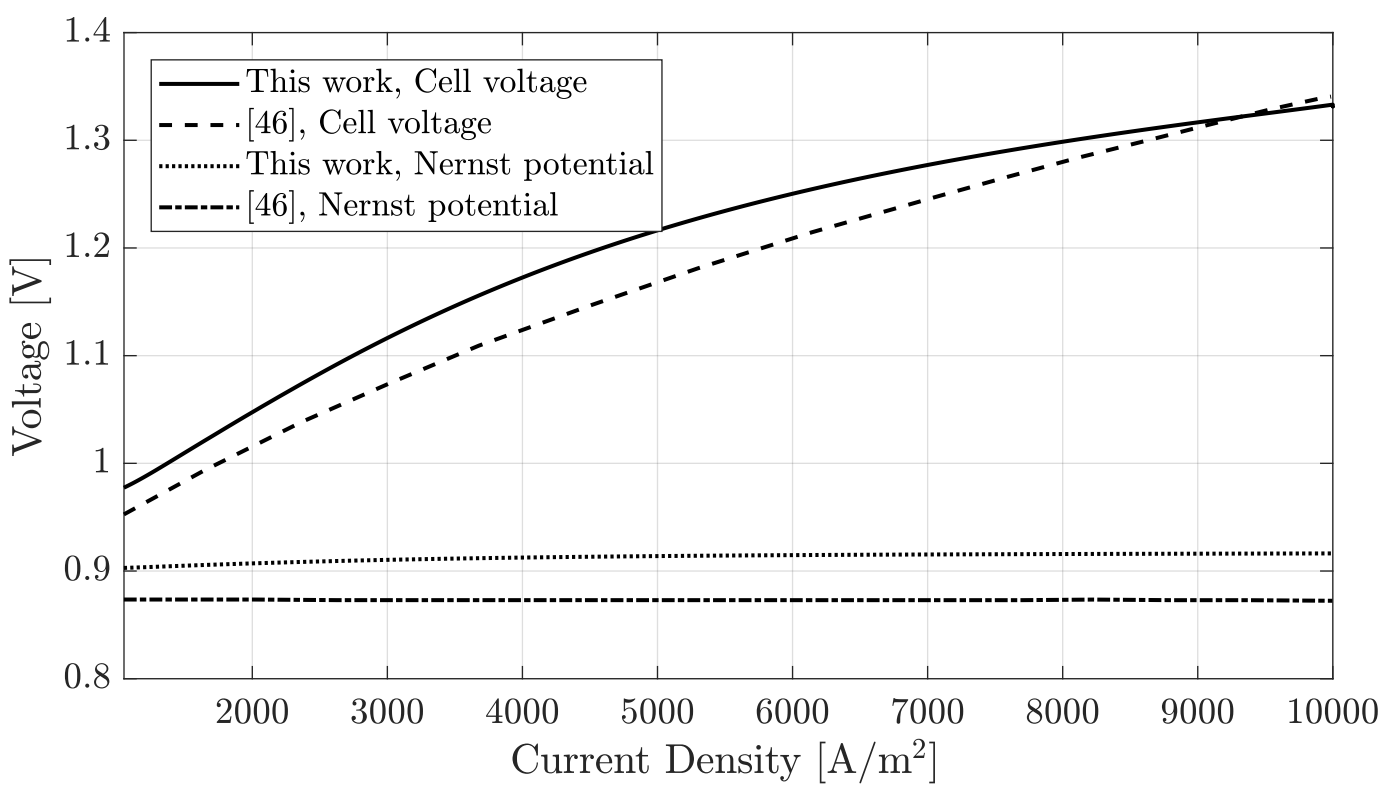
Table A. 1 input parameters used in the G(s) step response analysis

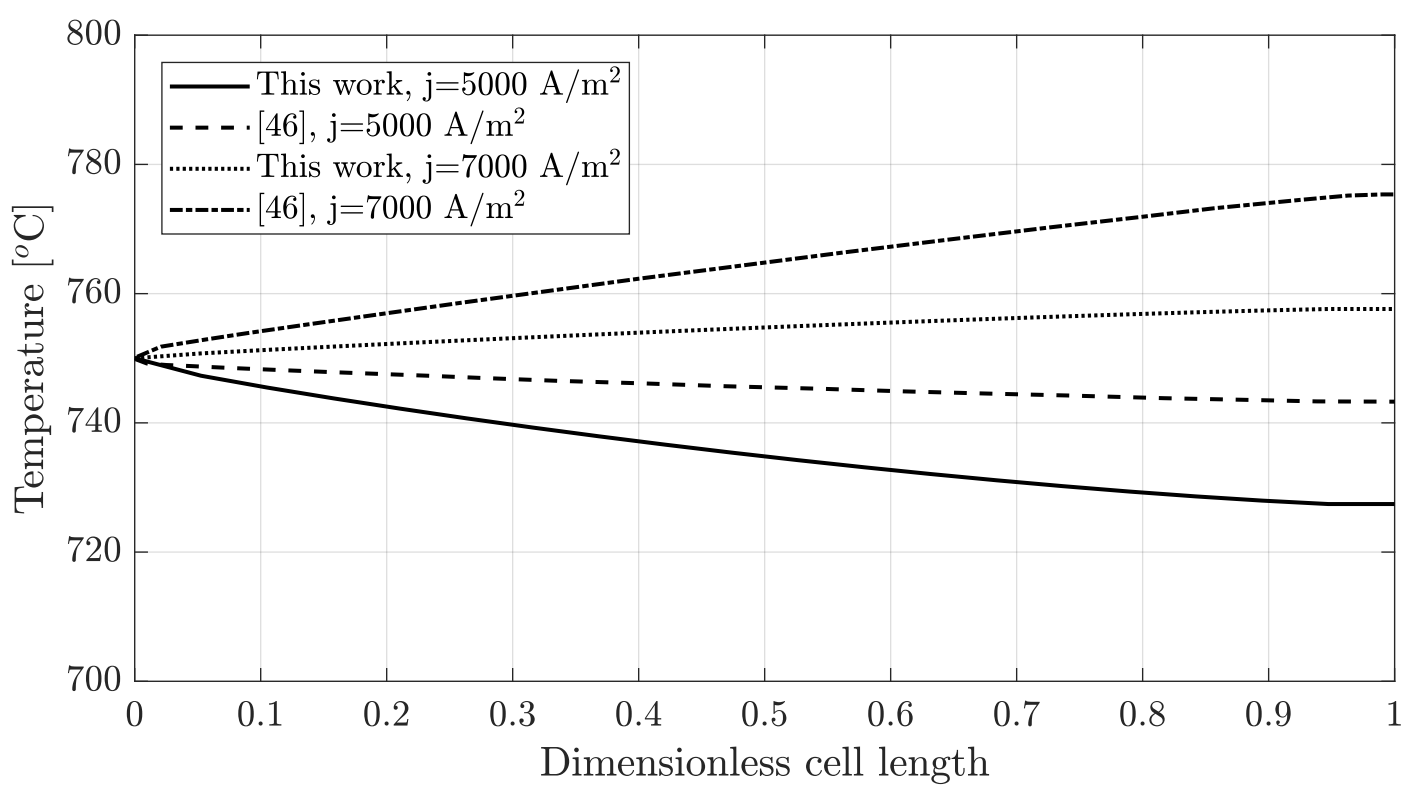
Stack parameters	
Stack mass [kg]	220
# of cells per substack [-]	50
# of substacks in the stack [-]	2
# of discretization volumes [-]	10
Cell parameters	
Cell area [m ²]	0.04
Cell length [m]	0.4
Cell thickness [μm]	500
Cell density, ρ_{cell} [kg/m ³]	5900
Total cell mass, m_{cell} [kg]	0.3
Specific heat capacity, c_p [kJ/kgK]	0.5
Reference ASR ₀ [Ωcm ²]	0.35×10^{-4}
Reference temperature, T ₀ [°C]	750
Activation energy, E _a [J/mol]	62715.5
Convective efficient solid-gas control volume	250
h_{conv} [W/m ² K]	
Fuel and air channel geometric parameters	
Fuel channel height [mm]	1
Air channel height [mm]	1
Interconnect thickness [μm]	500
Interconnect density, ρ_{int} [kg/m ³]	8000
Gas mixture condition at the SOEC and SOFC stacks inlet	
Pressure [bar]	1
H ₂ -H ₂ O inlet temperature [°C]	750
Air inlet temperature [°C]	750
Steam molar fraction [-]	0.45
Hydrogen molar fraction [-]	0.50

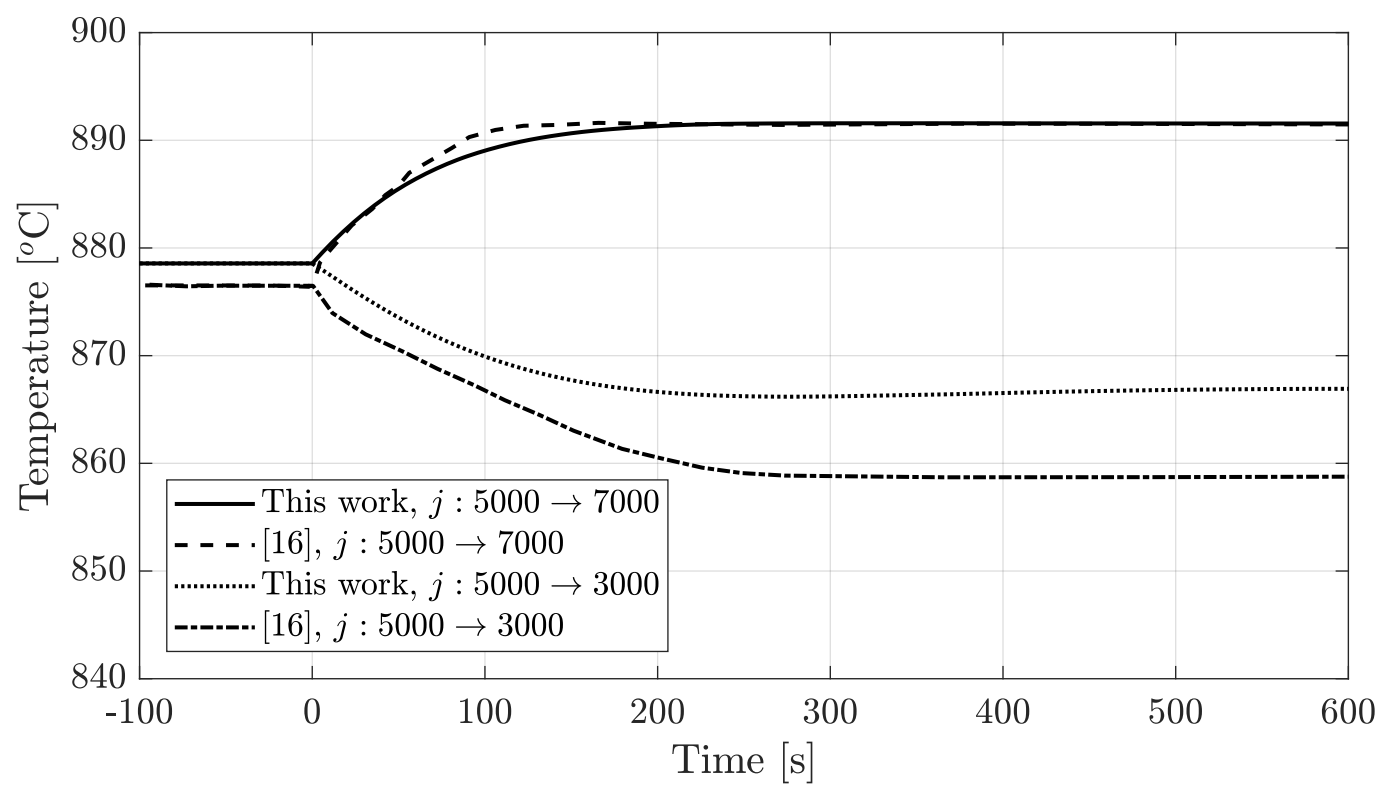
Inert gases in fuel electrode [-]	0.05
Fuel mass flow [kg/s] SOEC	9e-3
Fuel mass flow [kg/s] SOFC	5.83e-3
Air mass flow [kg/s] SOEC	4.75e-2
Air mass flow [kg/s] SOFC	1.91e-1
Stack operating conditions	
Current density evaluated SOEC [A/m ²]	13962
Current density evaluated SOFC [A/m ²]	6725

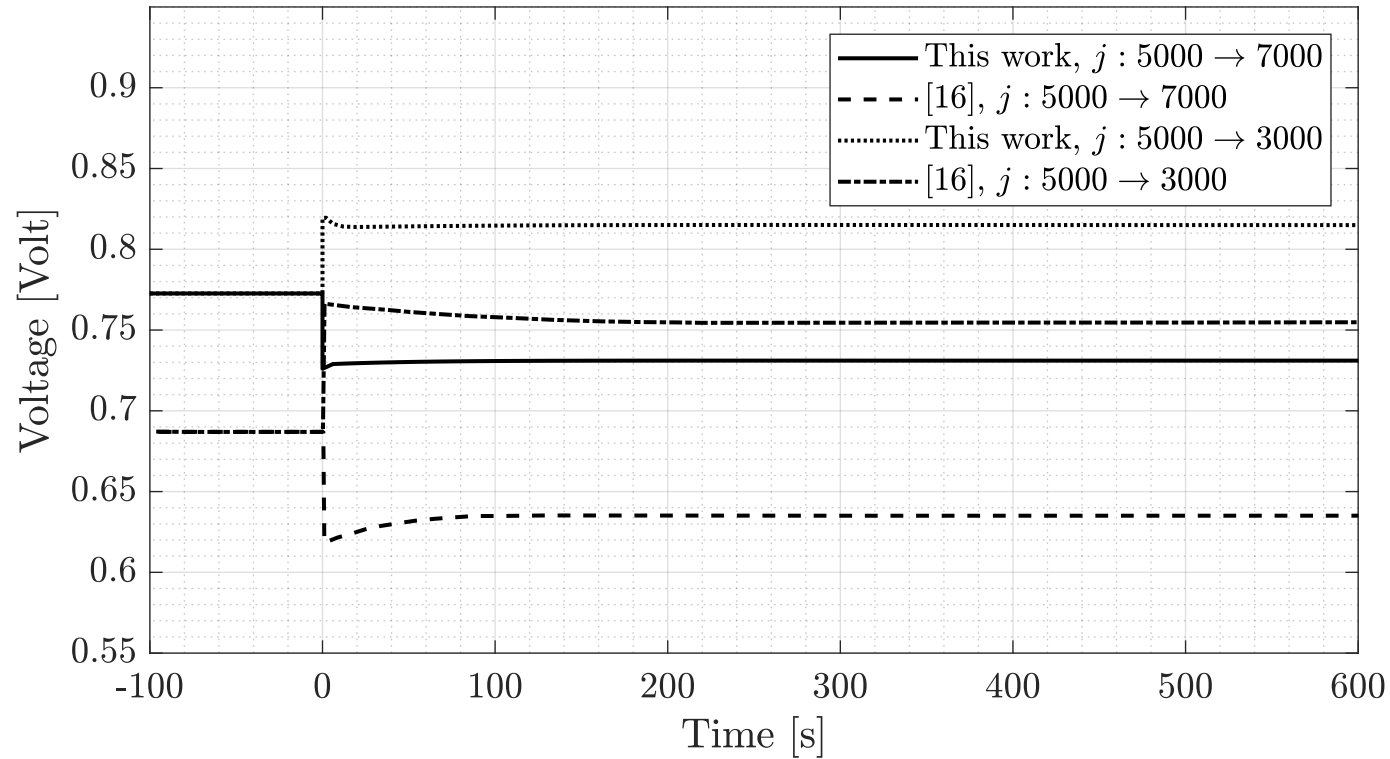


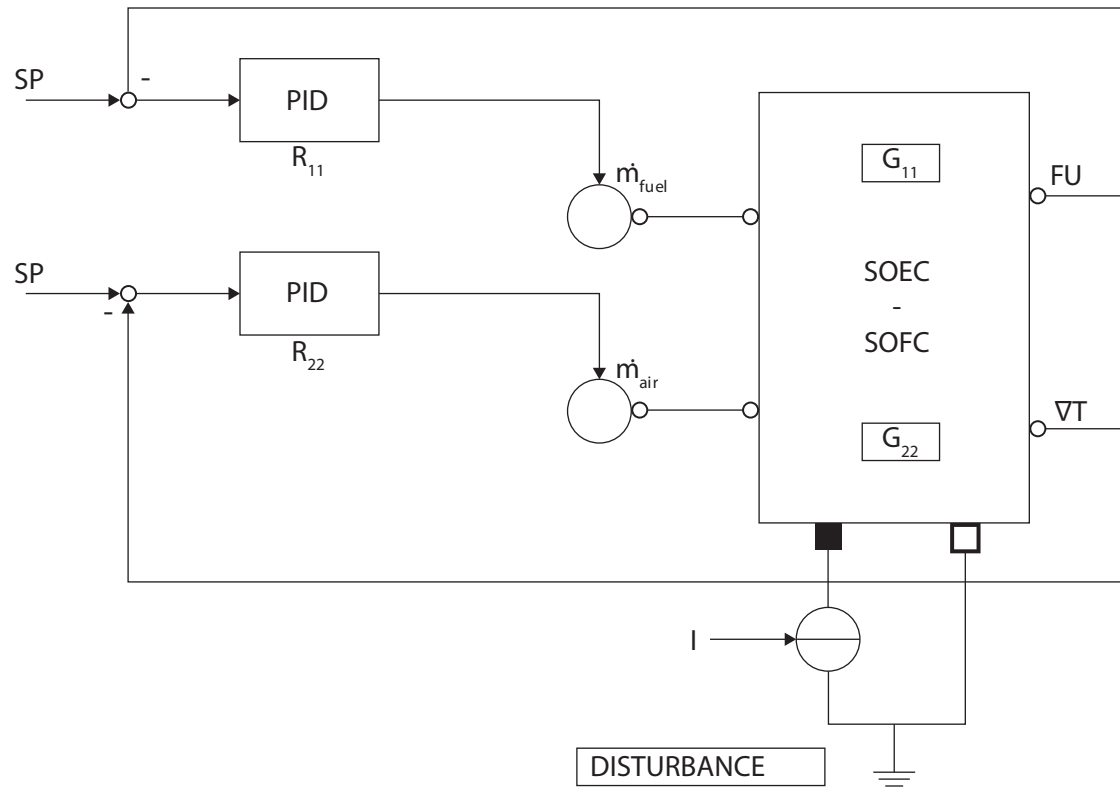




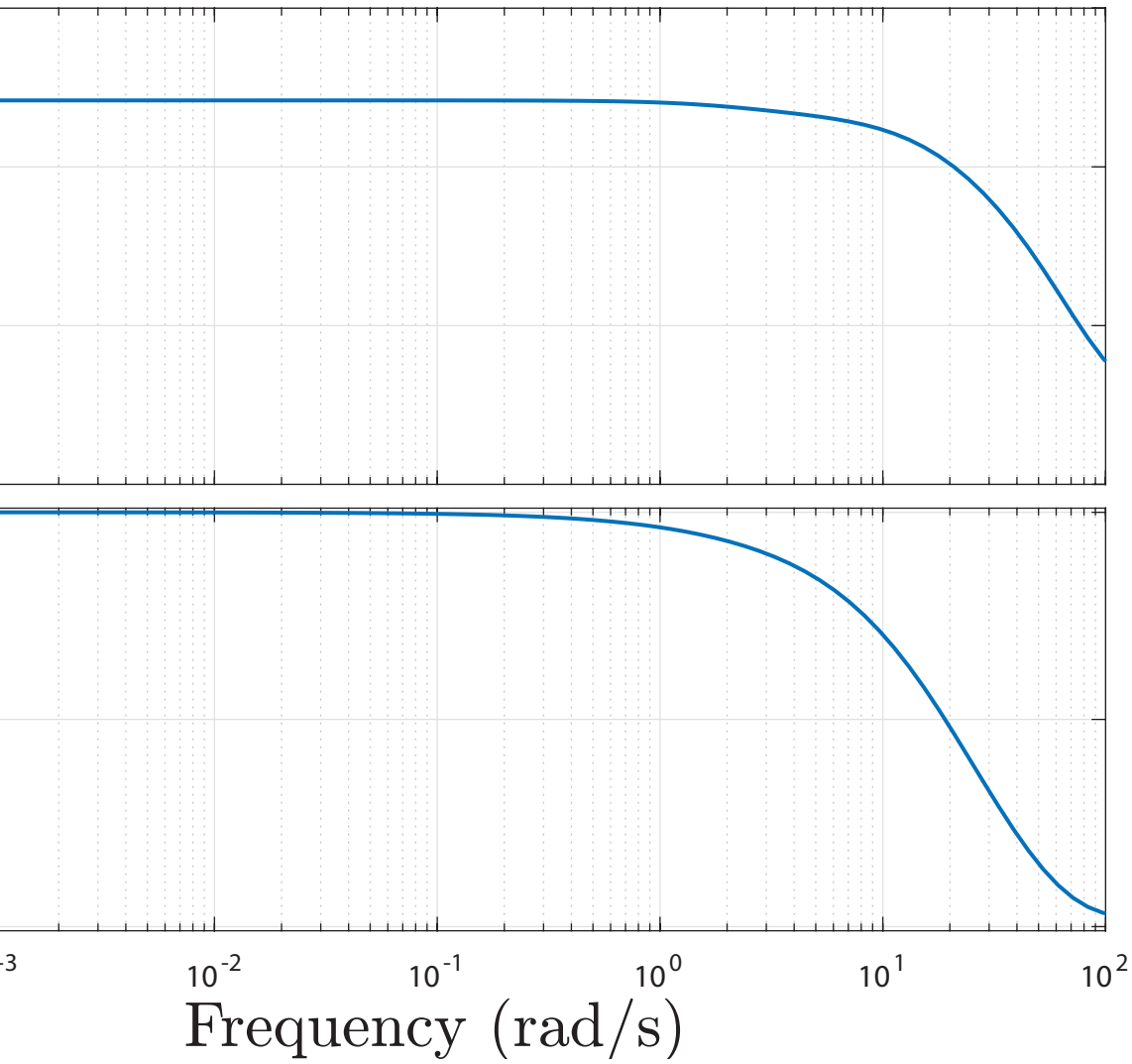




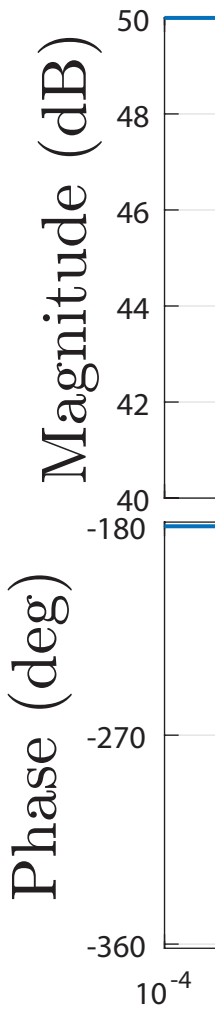




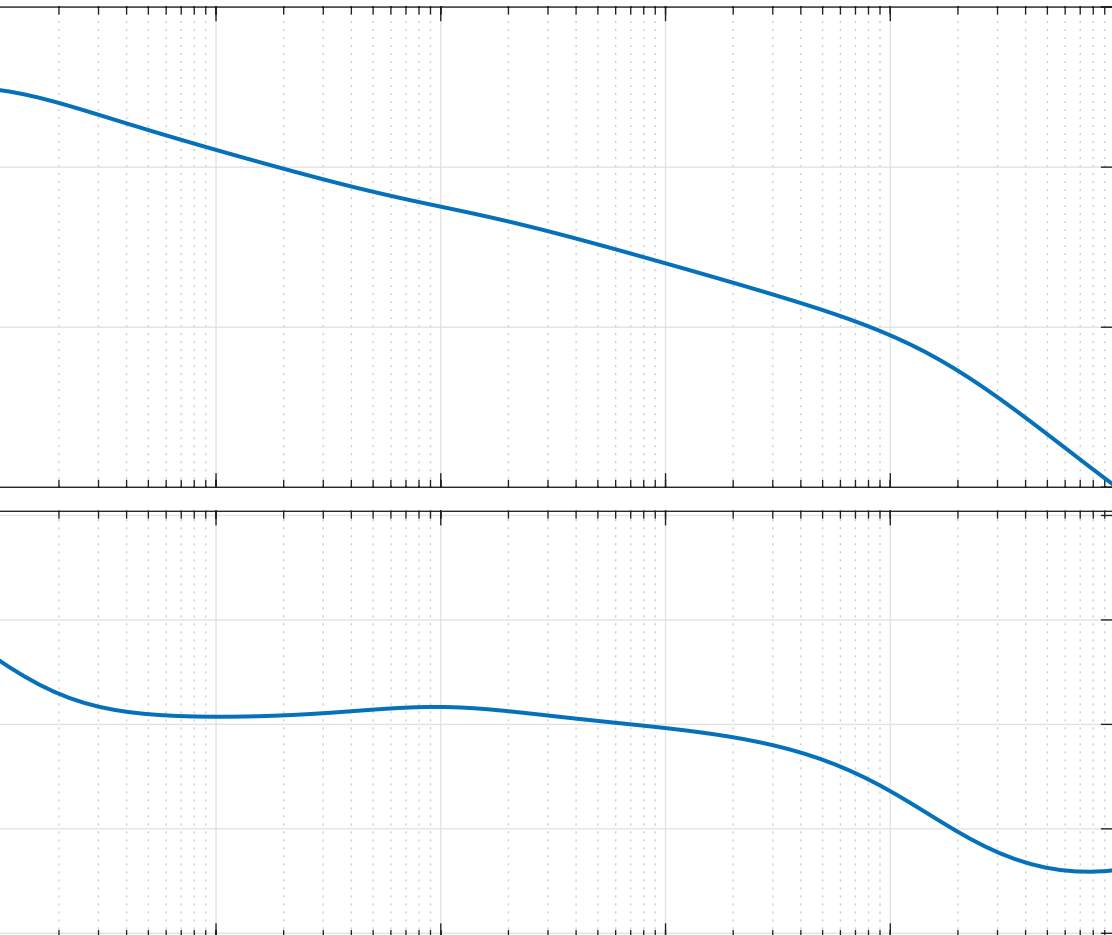
Bode Diagram



G11 SO



Bode Diagram



G22 SO

